Since January 2020 Elsevier has created a COVID-19 resource centre with free information in English and Mandarin on the novel coronavirus COVID-19. The COVID-19 resource centre is hosted on Elsevier Connect, the company's public news and information website.

Cell Reports

Article

RAI1 Regulates Activity-Dependent Nascent Transcription and Synaptic Scaling

Graphical Abstract

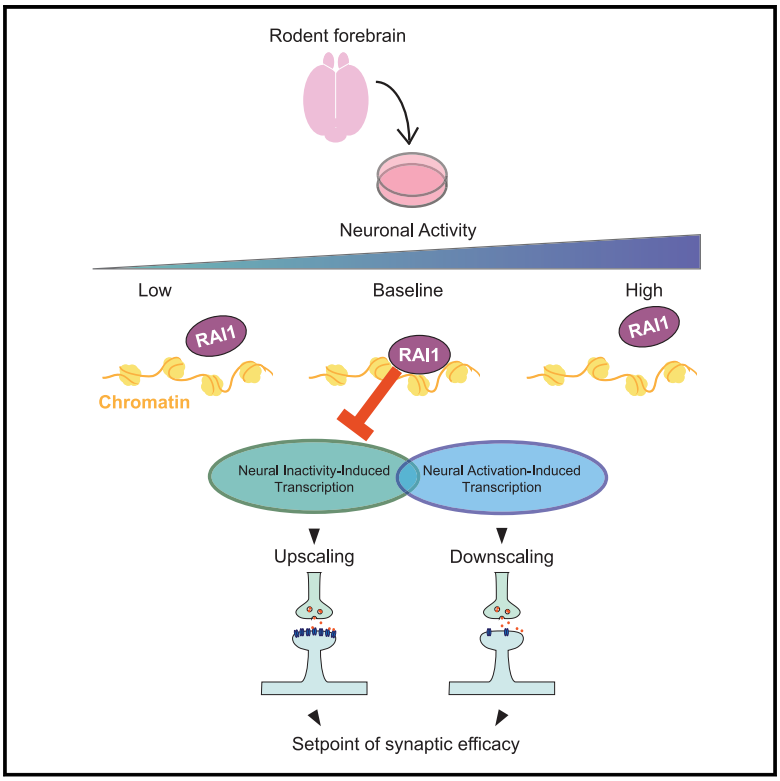

Highlights

- BrU-seq reveals nascent transcription during synaptic up- or downscaling
- Smith-Magenis syndrome protein RAI1 regulates upscaling-associated transcription
- RAI1 departs chromatin in response to network activity shifts
- RAI1 blocks upscaling in naive networks and promotes inactivity-induced upscaling

Authors

Patricia M. Garay, Alex Chen, Takao Tsukahara, ..., Kevin S. Jones, Michael A. Sutton, Shigeki Iwase

Correspondence

masutton@umich.edu (M.A.S.), siwase@umich.edu (S.I.)

In Brief

Garay et al. adopt BrU-seq to profile bona fide transcriptional dynamics triggered by neuronal activity shifts. An integrated genomics approach including BrU-seq, combined with electrophysiology, reveals that RAI1, the Smith-Magenis syndrome protein, controls baseline synaptic strength and homeostatic synaptic upscaling by regulating the transcriptome associated with network inactivity.

Garay et al., 2020, Cell Reports *32*, 108002
August 11, 2020
https://doi.org/10.1016/j.celrep.2020.108002

CellPress

Cell Reports

CellPress
OPEN ACCESS

Article

RAI1 Regulates Activity-Dependent Nascent Transcription and Synaptic Scaling

Patricia M. Garay,[1] Alex Chen,[1] Takao Tsukahara,[2,3,4] Jean Carlos Rodríguez Díaz,[1] Rafi Kohen,[1] J. Christian Althaus,[2,3] Margarete A. Wallner,[5] Roman J. Giger,[1,6,7,8] Kevin S. Jones,[1,9] Michael A. Sutton,[1,2,3,*] and Shigeki Iwase[1,4,10,*]

[1]Neuroscience Graduate Program, University of Michigan Medical School, Ann Arbor, MI 48109, USA
[2]Department of Molecular and Integrative Physiology, University of Michigan, Ann Arbor, MI 48109, USA
[3]Michigan Neuroscience Institute, University of Michigan, Ann Arbor, MI 48109, USA
[4]Department of Human Genetics, University of Michigan, Ann Arbor, MI 48109, USA
[5]College of Literature, Science, and the Arts, University of Michigan, Ann Arbor, MI 48109, USA
[6]Department of Cell and Developmental Biology, University of Michigan Medical School, Ann Arbor, MI, 48109, USA
[7]Cellular and Molecular Biology Graduate Program, University of Michigan Medical School, Ann Arbor, MI, 48109, USA
[8]Department of Neurology, University of Michigan Medical School, Ann Arbor, MI, 48109, USA
[9]Department of Pharmacology, University of Michigan Medical School, Ann Arbor, MI, 48109, USA
[10]Lead Contact
*Correspondence: masutton@umich.edu (M.A.S.), siwase@umich.edu (S.I.)
https://doi.org/10.1016/j.celrep.2020.108002

SUMMARY

Long-lasting forms of synaptic plasticity such as synaptic scaling are critically dependent on transcription. Activity-dependent transcriptional dynamics in neurons, however, remain incompletely characterized because most previous efforts relied on measurement of steady-state mRNAs. Here, we use nascent RNA sequencing to profile transcriptional dynamics of primary neuron cultures undergoing network activity shifts. We find pervasive transcriptional changes, in which ~45% of expressed genes respond to network activity shifts. We further link retinoic acid-induced 1 (RAI1), the Smith-Magenis syndrome gene, to the transcriptional program driven by reduced network activity. Remarkable agreement among nascent transcriptomes, dynamic chromatin occupancy of RAI1, and electrophysiological properties of *Rai1*-deficient neurons demonstrates the essential roles of RAI1 in suppressing synaptic upscaling in the naive network, while promoting upscaling triggered by activity silencing. These results highlight the utility of bona fide transcription profiling to discover mechanisms of activity-dependent chromatin remodeling that underlie normal and pathological synaptic plasticity.

INTRODUCTION

Proper cognitive development and brain function rely on synaptic plasticity, the ability of synapses to strengthen or weaken in response to sensory or neuromodulatory inputs. Synaptic scaling is one mechanism of plasticity, which buffers potentially destabilizing patterns of network activity (Abbott and Nelson, 2000; Miller and MacKay, 1994; Turrigiano, 2008). In response to a sustained increase in neuronal firing rate, neurons decrease, or ''scale down,'' the receptivity of the neuron to excitatory neurotransmitters. Conversely, global decreases in firing rate cause neurons to ''scale up'' and increase synaptic efficacy. Synaptic scaling can accommodate other forms of plasticity, such as long-term potentiation (LTP), that impose long-lasting increase of individual synaptic efficacy, which left uncompensated would result in circuits that are overly active (Turrigiano, 2017). Synaptic scaling plays important roles in neurodevelopment, learning, and memory (Fernandes and Carvalho, 2016; Yee et al., 2017). Dysregulated homeostatic plasticity is a common pathological hallmark in several neurodevelopmental disorders, including fragile X syndrome (Soden and Chen, 2010), Rett syndrome (Zhong et al., 2012), tuberous sclerosis (Bateup et al., 2013), Kleefstra syndrome (Benevento et al., 2016), and some autism spectrum conditions (Bourgeron, 2015).

Synaptic scaling requires *de novo* synthesis of RNAs and proteins that directly modulate synaptic efficacy (Benito and Barco, 2015; Ibata et al., 2008; Igaz et al., 2002). DNA-binding transcription factors (TFs), such as cyclic AMP-response binding protein (CREB), drive transcriptional responses to neuronal activation (West et al., 2002). The initial response is a rapid induction of immediate-early genes, such as *Arc* and *Homer1* (Brakeman et al., 1997; Bramham et al., 2008). The gene expression programs triggered by reductions in network activity involves distinct TFs, such as SRF and ELK1 (Schaukowitch et al., 2017).

In eukaryotic cells, transcriptional responses must occur in a refractory environment in which DNA is packaged into chromatin. The strong linkage between cognitive disorders and chromatin-regulatory genes suggests that activity-dependent chromatin reorganization is essential for proper brain development and mental health (Ebert and Greenberg, 2013; Guzman-Karlsson et al., 2014; Mullins et al., 2016). Indeed, activity-dependent gene expression underlying LTP and memory

requires chromatin regulators, such as histone acetyltransferases and deacetylases (Campbell and Wood, 2019). A handful of chromatin regulators, TET3 DNA demethylase (Yu et al., 2015b), EHMT1/2 histone H3K9 methyltransferases (Benevento et al., 2016), and L3MBTL1 methyl-histone binding factor (Mao et al., 2018) affect synaptic scaling. Yet these molecules constitute an infinitesimal fraction of the many chromatin regulators that have genetic links to neurodevelopmental disorders. We do not know the extent to which disease-associated chromatin regulators play roles in transcription-dependent synaptic plasticity.

Another unresolved issue is the precise mechanisms by which these chromatin regulators contribute to transcription. To dissect the mechanism, accurate monitoring of transcriptional responses is critical. Most prior studies have monitored steady-state mRNA levels, using qRT-PCR, cDNA microarray, and mRNA sequencing (mRNA-seq). The brain exhibits notorious complexity of post-transcriptional regulation, including activity-dependent mRNA splicing (Hermey et al., 2017), mRNA decay (Widagdo and Anggono, 2018), mRNA transport, and local translation (Glock et al., 2017). Therefore, reliance on steady-state mRNA measurements may obscure the roles of chromatin regulators in transcription.

In the present work, we developed genome-wide measurement of bona fide transcriptional dynamics in response to bidirectional network activity alterations. We then used this approach to uncover a role for the chromatin regulator retinoic acid-induced 1 (RAI1) in the transcriptional program. RAI1 is a nucleosome-binding protein (Darvekar et al., 2012, 2013) and is expressed throughout the embryonic and adult brain (Huang et al., 2016). *RAI1* is associated with two human intellectual disability syndromes. *RAI1* haploinsufficiency leads to Smith-Magenis syndrome (SMS; MIM: 182290), while *RAI1* duplication results in Potocki-Lupski syndrome (PTLS; MIM: 610883) (Bi et al., 2004; Girirajan et al., 2005; Potocki et al., 2007; Slager et al., 2003). Studies in mouse models and human patient cells have uncovered roles of RAI1 in gene expression, neuronal structure, and behavior (Bi et al., 2005, 2007; Huang et al., 2016, 2018; Lacaria et al., 2013). However, no study has described RAI1 in activity-dependent transcription and synaptic plasticity to date. We therefore explored the roles of RAI1 in activity-dependent transcription and synaptic scaling.

RESULTS

Altered Neuronal Network Activity Triggers Genome-wide Transcriptional Changes

To overcome the major limitation of steady-state RNA sequencing (RNA-seq), we adopted bromouridine sequencing (BrU-seq), a genome-wide profiling technique of nascent transcripts (Paulsen et al., 2013, 2014). We prepared primary forebrain neuron cultures from embryonic day 18 (E18) mouse embryos and allowed them to mature for 17 days *in vitro* (DIV). To monitor bidirectional transcriptional responses to activity shifts, network activity was elevated by 20 μM bicuculline (BIC; a $GABA_A$ receptor antagonist) or suppressed by 1 μM tetrodotoxin (TTX; a sodium channel blocker) for 4 h. During the last 20 min of BIC or TTX treatment, we added BrU to the culture medium to label newly synthesized transcripts. We isolated the labeled RNAs using an anti-BrU antibody and subjected them to next-generation sequencing (Figure 1A).

Our BrU-seq dataset demonstrated the expected induction of *Arc* and *Fos* by BIC (Figure 1B). Abundant intronic reads indicate that detected transcripts were recently generated and yet to be spliced. Other well-characterized activity-dependent genes, such as *Npas4*, *Egr1*, *Homer1*, *Tet3*, and *Txnip*, also showed expected transcriptional induction (Table S1). Differential gene expression analysis of the BrU-seq data using DESeq2 (Love et al., 2014) revealed widespread transcriptional changes, in which 45% of expressed genes (7,592 of 16,682) were up- or downregulated by network activity shifts ($p_{adj} < 0.05$; Figure 1C). BIC increased transcription of 2,908 genes, while TTX did so for 1,820 genes. The magnitude of transcriptional induction is higher with BIC treatment compared with TTX treatment (Figure 1D). To examine the relationship between nascent and steady-state transcriptomes, we compared our BrU-seq data with published mRNA-seq datasets of mouse cortical neurons treated with TTX or BIC for 4 or 6 h (Schaukowitch et al., 2017; Yu et al., 2015b) with identical data processing. Our 4 h BrU-seq results showed a much stronger similarity with 4 h mRNA-seq than 6 h mRNA-seq data (Figure S1B). Thus, BrU-seq reliably captures known transcriptional responses to bidirectional shifts in network activity.

BrU-seq might be a better approach than mRNA-seq to detect downregulation of transcription, because the persistence of RNAs after transcription does not contribute to BrU-seq signals. Indeed, we found significantly larger suppression of *Fos*, *Arc*, *Bdnf*, and *Npas4* (4- to 16-fold) by TTX treatment in BrU-seq compared with mRNA-seq performed with 4 h BIC and TTX treatments, in which downregulation was less than 2-fold (Figure 1E) (Schaukowitch et al., 2017; Yu et al., 2015b). The magnitude of upregulation in response to BIC was smaller in BrU-seq, likely because the early transcriptional induction is largely complete 4 h after BIC treatment. At a genome-wide scale, BrU-seq allowed us to detect transcriptional suppression of numerous genes (BIC, n = 2,842; TTX, n = 2,307). These data highlight an advantage of the BrU-seq approach to probe mechanisms underlying highly dynamic activity-dependent transcription.

On the basis of the behavior of well-defined activity-response genes (Figure 1E), one could assume that BIC and TTX trigger reciprocal transcriptional responses. Unexpectedly, only a small fraction of activity-response genes (24% [1,798 of 7,592]) displayed such mirrored responses between BIC and TTX treatments (Figure 1F). Six percent of activity-response genes (487 of 7,592) altered their transcription levels in the same direction after BIC and TTX treatments. The remaining majority of genes (70% [5,307 of 7,592]) responded to BIC or TTX uniquely. These data suggest that synaptic up- and downscaling involves distinct transcriptional programs. Table S1 lists genes that displayed greater than 2-fold changes in transcription upon network activity shifts.

Recent studies have reported that different cell types, such as astrocytes and neuronal subtypes, induce distinct sets of genes in an activity-dependent manner (Hasel et al., 2017; Hrvatin et al., 2018). We sought to assess the contribution of various cell types in our datasets. Using immunocytochemistry of a set of cell type markers, NeuN, GAD67, GFAP, CD11b, and Olig2, we estimated that our cultures comprise 41% excitatory neurons, 11%

CellPress
OPEN ACCESS

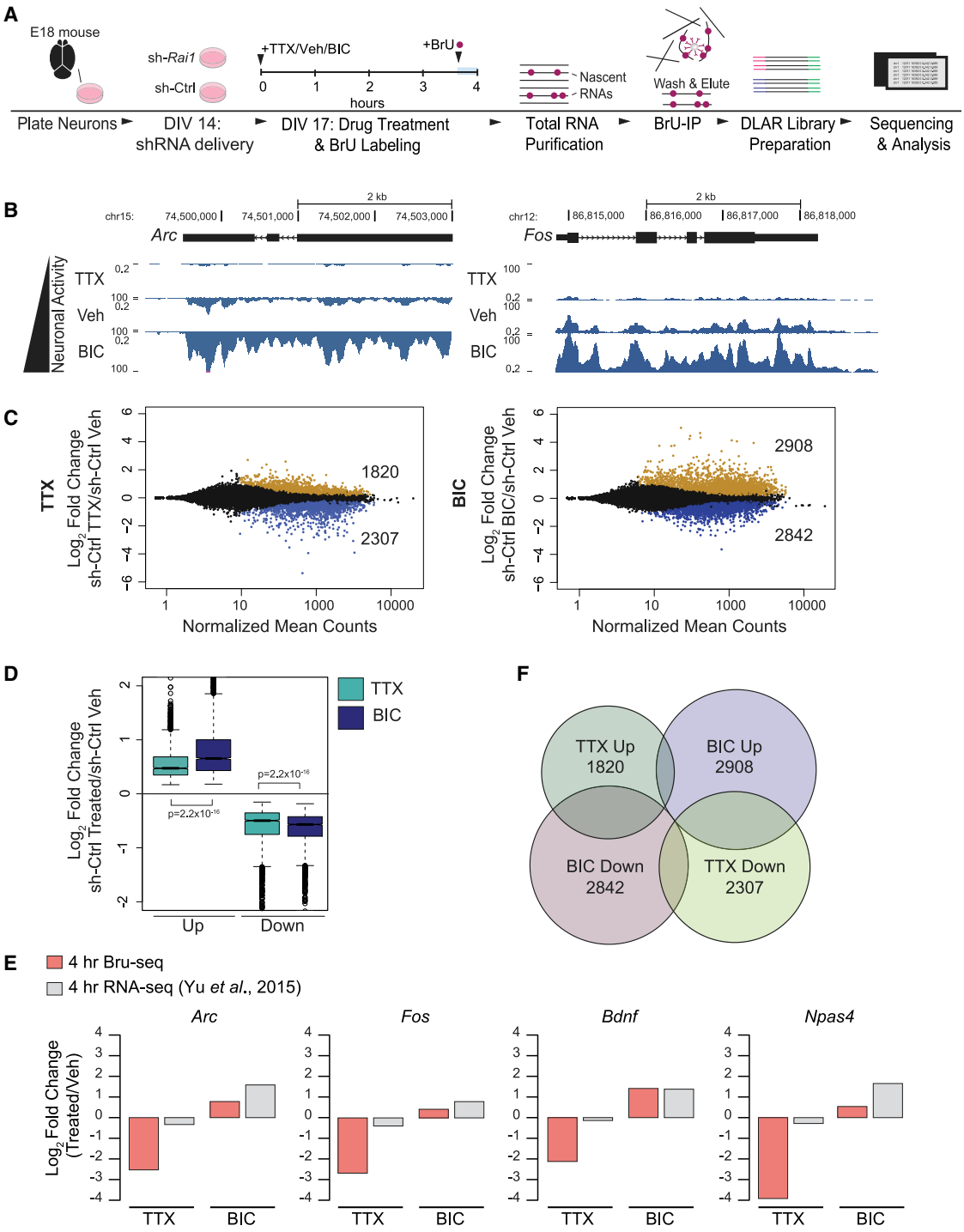

Figure 1. Genome-wide Transcriptional Response to Bidirectional Activity Alterations

(A) Experimental procedure.

(B) UCSC Browser views of BrU-seq signals at *Arc* and *Fos*. Intronic reads are characteristic of nascent RNA.

(C) Differential gene expression analysis (DESeq2) reveals widespread transcriptional changes in response to TTX and BIC ($p_{adj} < 0.05$).

(D) BIC-response genes show a greater median fold change (Wilcoxon rank-sum test). Whiskers represent 1.5 times the inter-quartile range (IQR), and the notch represents the 95% confidence interval of the median.

(E) Downregulation of immediate-early gene in the TTX condition is captured more sensitively in BrU-seq data compared with mRNA-seq data (Yu et al., 2015b).

(F) The majority of TTX and BIC response genes are uniquely regulated (70%). 24% of genes are reciprocally regulated, and 6% are commonly regulated.

See also Figure S1 and Tables S1 and S2.

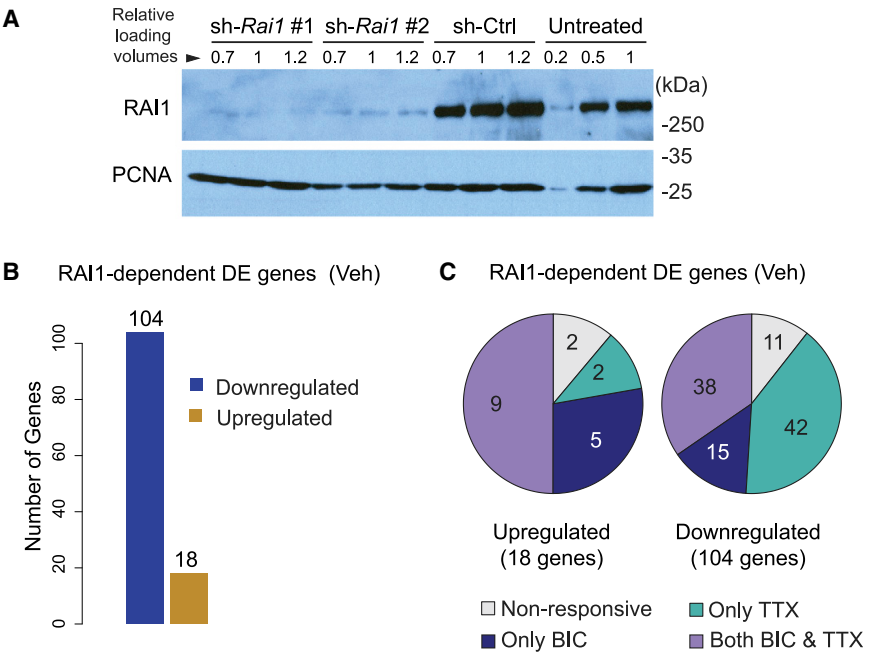

Figure 2. *Rai1* KD Alters Transcription of TTX-Response Genes at Baseline

(A) Validation of *Rai1* KD with western blot. Mouse forebrain neuron cultures were transduced with lentivirus expressing sh-*Rai1* or sh-Ctrl for 3 days.

(B) Number of DESeq2-called differentially expressed genes (sh-Ctrl versus sh-*Rai1*, $p_{adj} < 0.05$) after vehicle treatment.

(C) Many *Rai1*-KD DE genes are TTX- and BIC-response genes.

(D) The fold changes of TTX- and BIC-response genes by *Rai1* KD at baseline. Note that *Rai1*-KD cultures display a transcriptional profile similar to TTX-treated control cultures. r, Spearman's rank correlation coefficient.

See also Figure S2 and Tables S3 and S4.

inhibitory neurons, 33% astrocytes, 15% of cells within the oligodendrocyte lineage, and no microglia (Figures S1D and S1E). We found several non-neuronal genes in our dataset, including *Thbs1*, a synaptic regulator expressed specifically in astrocytes (Risher and Eroglu, 2012). We detected enrichment of biological processes specific for both neurons and non-neuronal cell types (Table S2). Intersection of the BrU-seq data with published cell-type-enriched genes (Zhang et al., 2014) revealed that the majority (>80%) of the activity-response genes do not exhibit cell type-specific expression (Figure S1F). Thus, the present dataset represents an aggregate view of transcriptional response occurring in multiple cell types.

RAI1 Suppresses the TTX-Induced Transcriptional Program in Resting Networks

RAI1 is one of many chromatin regulators that are mutated in neurodevelopmental disorders. Little is known about RAI1's roles in activity-dependent transcription and synaptic plasticity. We developed an anti-RAI1 antibody and confirmed that RAI1 protein was present in virtually all MAP2-positive neurons and primarily localized to the nucleus, with subtle signals in the soma (Figure S2A). We found lower RAI1 levels in non-neuronal (MAP2-negative) cell nuclei (Figure S2A), highlighting its important role in neurons. Widespread presence of RAI1 in neurons is consistent with previous studies (Fragoso et al., 2014; Huang et al., 2016) (Figures S2B and S2C).

Having established nascent transcriptional profiling in neural ensembles and the presence of RAI1 in our cultures, we sought to test if RAI1 has any roles in synaptic scaling and transcriptional responses to altered neuronal activity. We knocked down *Rai1* in primary cortical cultures using lentiviral vectors (LVs) carrying *Rai1* or scrambled short hairpin RNAs (shRNAs) (sh-Ctrl). To minimize the impact of RAI1 loss on network connectivity, we delivered LV shRNA at DIV 14, a time by which functional synapses have formed. The knockdown (KD) achieved near complete loss of RAI1 protein by 3 days post-LV infection (Figure 2A). We then modulated network activity of LV-treated cultures by applying TTX or BIC for 4 h and carried out BrU-seq as described above.

We initially tested if *Rai1* KD alters nascent transcription in control "resting" neuronal cultures with stable basal levels of activity. DESeq2 analysis revealed 122 differentially expressed (DE) genes: 104 downregulated and 18 upregulated following *Rai1* KD ($p_{adj} < 0.05$; Figure 2B; Table S3). The finding that *Rai1* KD downregulates more genes than it upregulates is consistent with the previous studies on RAI1 (Elsea and Williams, 2011; Huang et al., 2016). A majority of genes altered by *Rai1* KD at baseline were BIC- or TTX-response genes (Figure 2C). To further characterize the relationship between RAI1 deficiency and BIC- or TTX-response genes, we examined how individual

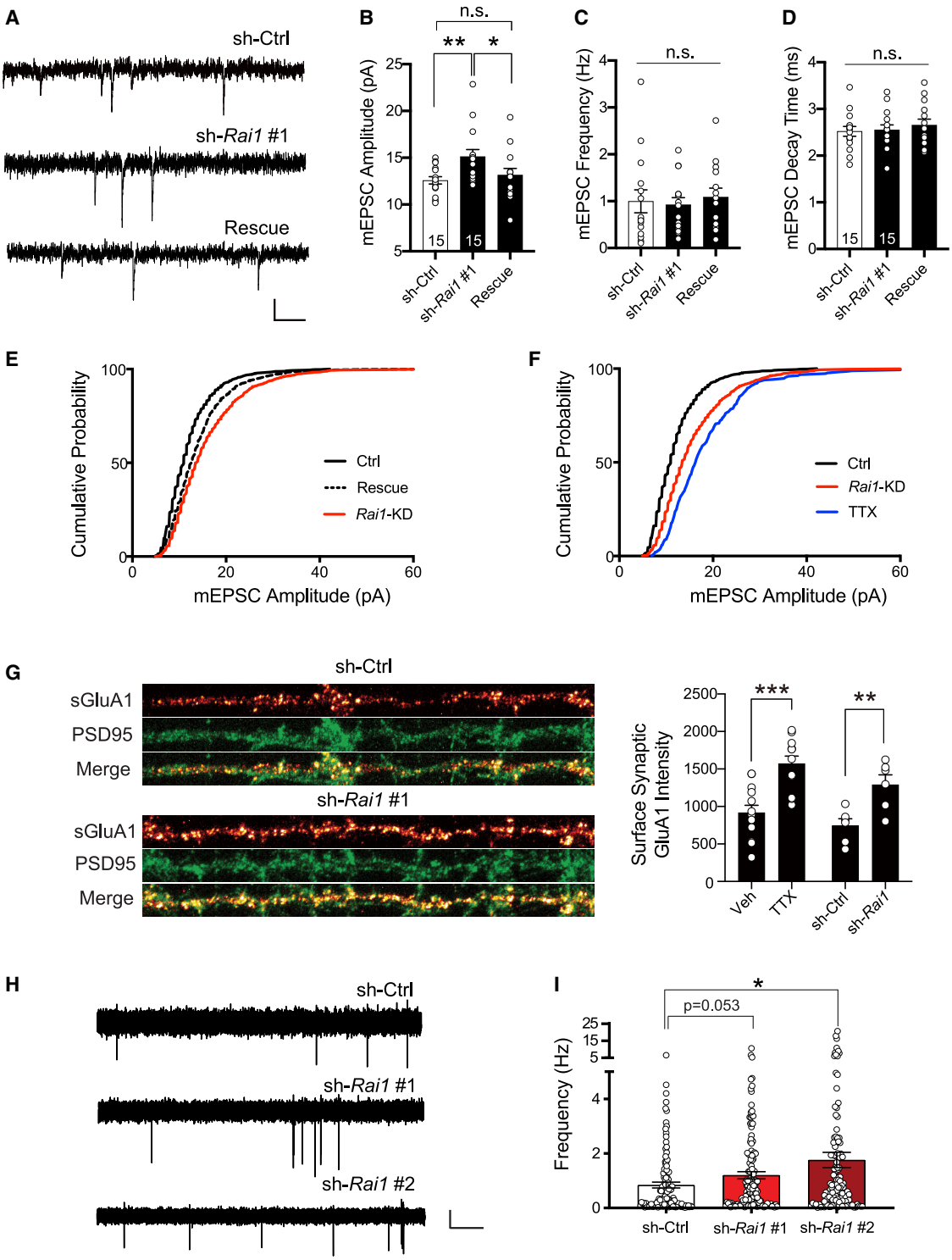

Figure 3. *Rai1* KD Increases Synaptic Efficacy at Baseline Activity Condition

(A–D) Example traces (A) and mean ± SEM mEPSC amplitude (B), frequency (C), and decay time (D) for cultured rat hippocampal primary neurons recorded after transient transfection (48 h) with non-targeting shRNA (sh-Ctrl), *Rai1* targeting shRNA, or sh-*Rai1* #1 with RNAi-resistant *Rai1*-expressing construct (rescue) at DIV 12–14. Scale bar, 10 pA, 75 ms (sh-Ctrl, sh-*Rai1* #1, and Rescue, n = 15, 15, and 14, respectively).

(E) Cumulative distribution of mEPSC amplitudes of sh-Ctrl (left), sh-*Rai11* (middle), and rescue (right) transfected neurons.

(F) Cumulative distribution of mEPSC amplitudes of sh-Ctrl-transfected neurons treated by either vehicle or 1 μM TTX (left) and sh-Ctrl or sh-*Rai1*-transfected neurons (right).

(legend continued on next page)

genes behave upon *Rai1* KD. We found a clear positive correlation between the normal transcriptional response to TTX and the transcriptional impairment by *Rai1* KD at baseline (Spearman rank correlation coefficient r = 0.53, t test p = 2.2×10^{-16}; Figure 2D, left panel). BIC-response genes showed no correlation with *Rai1* KD (Figure 2D, right panel). The group of genes that respond reciprocally to TTX and BIC (Figure 1F) showed a similar correlation as there was with all TTX-responsive genes (Figure S2D). When we removed all DE genes upon *Rai1* KD from the plot, the correlation remained significant (r = 0.52, p = 2.2×10^{-16}; Figure S2E), suggesting that the DE genes are not the sole driver for the observed correlation. We also analyzed the published mRNA-seq of the *Rai1*-knockout (KO) cortices (Huang et al., 2016) and found a similar trend in expression pattern of the TTX- and BIC-response genes *in vivo* (Figure S2F). These data show that RAI1 deficiency shifts the transcriptional profile toward the TTX-treated state without drug application and that *Rai1* KD does not affect transcription of non-reciprocal BIC-responsive genes.

RAI1 Deficiency Promotes Synaptic Upscaling

Chronic perturbation of neuronal activity by BIC or TTX induces decreases and increases in synaptic strength, which respectively underlie homeostatic synaptic downscaling and upscaling (Abbott and Nelson, 2000; Miller and MacKay, 1994; Turrigiano, 2008). Given that *Rai1* KD shifted the nascent transcriptome toward the TTX-like state, we asked whether *Rai1* KD would similarly shift excitatory synapse function toward a state similar to synaptic upscaling. We used sparse transfection of DIV 12–14 hippocampal cultures with either *Rai1* or scrambled shRNA and recorded miniature excitatory postsynaptic currents (mEPSCs) from transfected pyramidal-like neurons 48 h later. If *Rai1* KD induces synaptic strengthening in a cell-autonomous manner, we would expect to see a rightward shift in the distribution of mEPSC amplitudes as is observed during synaptic upscaling following chronic activity suppression with TTX. Consistent with this idea, we found that the expression of two distinct shRNAs targeting *Rai1* mRNA each induced a significant increase in baseline mEPSC amplitude (Figures 3A and 3B), without significantly altering mEPSC frequency or decay time (Figures 3C and 3D; Figures S3A–S3E). Moreover, *Rai1* KD induced a clear rightward shift in the cumulative probability distribution of mEPSC amplitudes relative to control neurons (Figure 3E; Figure S3E), an effect that was significantly (albeit partially) rescued by expression of RNAi-resistant RAI1 (F[2, 41] = 4.452, p = 0.017; sh-Ctrl, sh-*Rai1* #1, and rescue, n = 15, 15, and 14; sh-Ctrl versus sh-*Rai1* #1, p = 0.068; sh-*Rai1* #1 versus rescue, p = 0.0359; sh-Ctrl versus sh-*Rai1* #2, n = 14-13, p = 0.0012; Figures 3A–3E). The shift in distribution of mEPSC amplitudes with *Rai1* KD bears a striking similarity to changes in mEPSC distributions following chronic TTX treatment (Figure 3F), although *Rai1* KD did not shift mEPSC amplitudes to quite the same degree as TTX. An increase in surface expression of AMPA receptors (AMPARs) at synapses is a signature of synaptic upscaling following activity suppression. Consistent with previous observations, surface expression of the GluA1 AMPAR subunit at PSD-95-labeled excitatory synapses is significantly increased following long-term (24 h) TTX treatment (sh-Ctrl vehicle [Veh] versus TTX, n = 13-12, p = 0.0019; Figure 3G); likewise, we found a similar enhancement of surface GluA1 at synapses following 72 h *Rai1* KD (sh-Ctrl versus sh-*Rai1*, n = 6-6, p = 0.0065; Figure 3G). Together, these results suggest that reduced *Rai1* expression induces functional changes in excitatory synaptic function that mimic synaptic upscaling induced by activity suppression.

Two scenarios could explain the increase in mEPSC amplitude by *Rai1* KD accompanied by TTX-like transcription in resting neurons. The first possibility is that *Rai1* KD suppresses network activity, which in turn indirectly promotes a TTX-like transcriptional program and synaptic upscaling. An alternative possibility is that release of RAI1-mediated suppression of a TTX-responsive transcriptional program directly upscales synapse function. To distinguish these possibilities, we measured ongoing basal network activity of control hippocampal cultures and *Rai1* KD cultures using 60-channel microelectrode arrays (MEAs; Figures S3F and S3G). On DIV 11, we transduced the cultures with LV control or *Rai1* shRNA and recorded network activity on DIV 14. We used semi-automatic principal-component analysis to sort individual neuronal units (Figures S3H–S3K). If the changes in mEPSCs and transcriptional dynamics are an indirect effect secondary to *Rai1* KD suppressing network activity, then we would predict a marked decrease in neural firing. Contrary to this prediction, *Rai1* KD did not suppress firing in the network and instead led to 1.4- to 2.1-fold increase in spontaneous firing rate compared with scrambled shRNA (Figures 3H and 3I; Kruskal-Wallis test: 9.36, p = 0.009; Dunn's post hoc test: sh-Ctrl versus sh-*Rai1* #1, p = 0.053; sh-Ctrl versus sh-*Rai1* #2, p = 0.010), likely because of enhanced excitatory drive that accompanies *Rai1* KD-mediated synaptic strengthening. These data thus support the second explanation, whereby RAI1 suppresses a TTX-responsive transcriptional program and synaptic upscaling in naive neural networks.

RAI1 Promotes Transcriptional Responses Triggered by Reductions in Network Activity

Having uncovered that RAI1 was essential to suppress the TTX-associated transcriptional program under basal activity

(G) Representative images of surface GluA1 (sGluA1, fire), PSD-95 (green), and sGluA1 and PSD-95 (merge) of sh-Ctrl and sh-*Rai1*-infected dendrites. Scale bar, 10 μm. Bar graph of mean sGluA1 signal intensity in PSD-95-positive regions for vehicle or TTX (n = 13-12) and sh-Ctrl or sh-*Rai1* (n = 6-6) treated neurons.
(H) Prototypical local field potential recordings from individual electrodes exhibiting a single neuronal unit from cultures transfected with: sh-Ctrl, sh-*Rai1* #1, or sh-*Rai1* #2 lentivirus. Scale bars, 500 ms (x axis) and 20 μV (y axis).
(I) Firing frequency of individual neuronal units recorded from cultures transfected with sh-Ctrl, sh-*Rai1* #1, or sh-*Rai1* #2 (n = 115, 140, and 131 for sh-Ctrl, sh-*Rai1* #1, and sh-*Rai1* #2, respectively).
All bar graphs represent mean ± SEM. For (B)–(D), one-way ANOVA, followed by post hoc Fisher's least significant difference (LSD) test were performed. For (G), unpaired Student's t tests were performed. For (I), Kruskal-Wallis (K-W) test followed by post hoc Dunn's multiple-comparisons test was performed. K-W: 9.358, p = 0.0003. *p < 0.05, **p < 0.01, and ***p < 0.001. See also Figure S3.

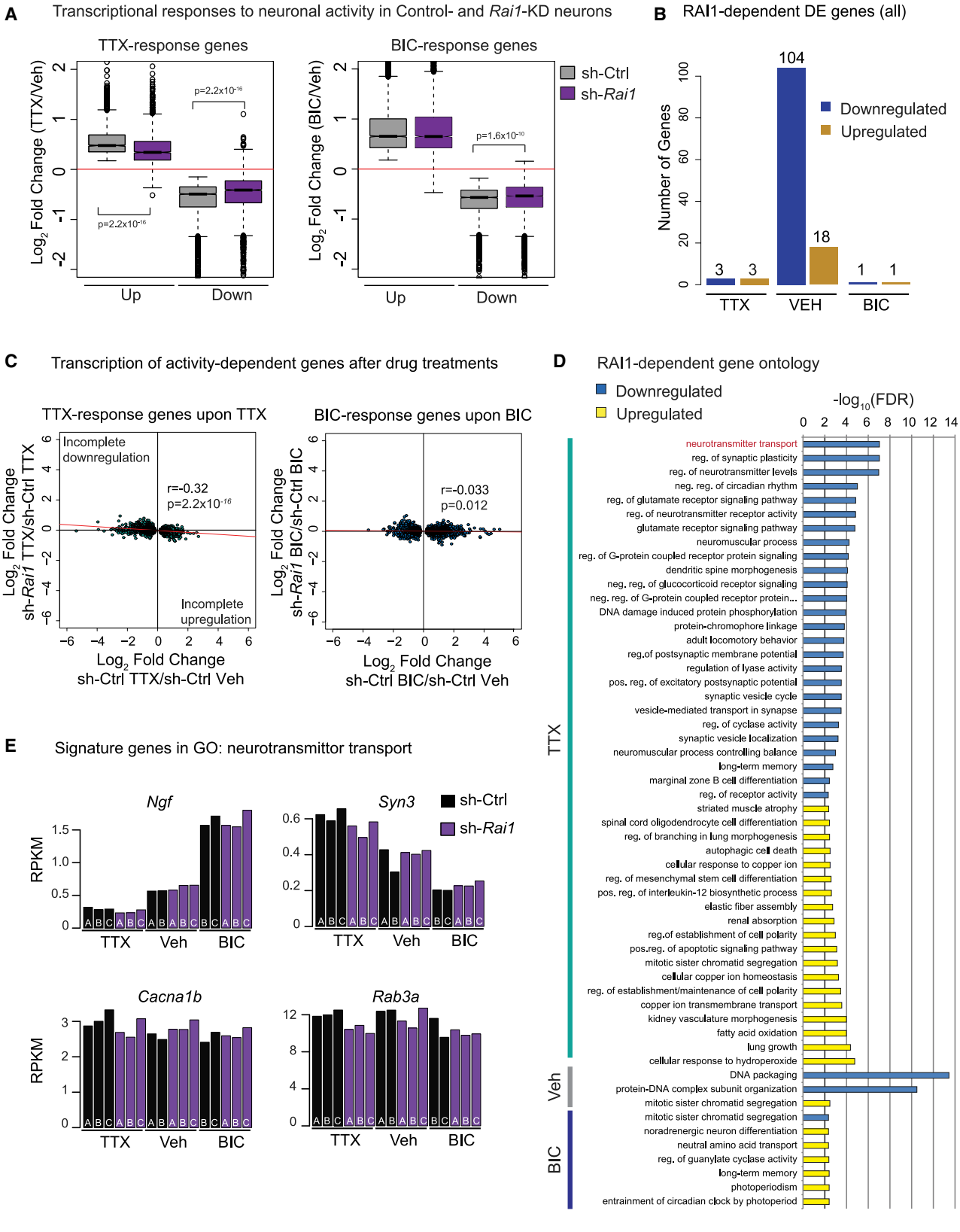

(legend on next page)

conditions (Figure 2), we next tested if *Rai1* KD has any impact on transcriptional responses to TTX and BIC treatments. By calculating fold changes of transcription, we found that *Rai1* KD led to a significant impairment of transcriptional response to TTX, while transcriptional responses to BIC were slightly weaker only for downregulation (Figure 4A). However, in contrast to the 130 genes transcriptionally altered at baseline, DESeq2 comparing *Rai1* KD and control revealed only 8 DE genes after TTX or BIC treatment, indicating that the impact of *Rai1* KD is greater in resting neurons compared with drug-treated neurons (Figure 4B; Table S3).

We then sought to determine if the strongly impaired transcriptional response to TTX (Figure 4A) was due entirely to the TTX-like transcriptional state of *Rai1*-KD cultures at baseline or if RAI1 also contributes to the transcriptional response to TTX. Differential gene expression analysis by DESeq2 relies on an arbitrary statistical significance cutoff to report DE genes. However, the individual gene plot in the baseline condition revealed a global transcriptional trend resulting from minor changes in many genes, including those that failed to achieve statistical significance (Figure S2E). To define the impact of RAI1 loss after TTX and BIC treatment, we therefore used this individual gene plot approach. We found that after TTX treatment, the transcriptional changes of TTX-response genes in *Rai1*-KD cultures inversely correlated with their changes upon TTX treatment in the control condition (Figure 4C, left panel; Spearman rank correlation coefficient $r = 0.32$, t test $p = 2.2 \times 10^{-16}$). This result indicates incomplete downregulation and upregulation upon TTX treatment independent of the impact of *Rai1* KD in the resting state. The same TTX-response genes did not show obvious changes after BIC treatment of *Rai1*-KD culture (Figure S4A, left panel). Transcription of the BIC-response genes did not show changes by *Rai1* KD under any condition (Figure 4C, right panel; Figure S4A, right panel). Thus, *Rai1* deficiency leads to a subtle yet widespread impairment of the transcriptional response to TTX but not to BIC. Taken together, these results led us to conclude that RAI1 is selectively required for the transcriptional response driven by network activity suppression.

We then explored biological implications for the impaired transcriptional response to TTX. We used RNA-Enrich, a Gene Ontology algorithm, which takes into account weaker changes in gene expression (Kim et al., 2012; Lee et al., 2016). Notably, RNA-Enrich identified many more RAI1-dependent biological processes after TTX treatment than vehicle or BIC treatment (45 in TTX-treated cultures, 3 in Veh-treated cultures, and 7 in BIC-treated cultures; Figure 4D). The p_{adj} values were evidently lower in the post-TTX transcriptome data compared with BIC conditions. The RAI1-dependent gene ontologies after TTX treatment represent synapse-related processes, whereas those altered in the BIC and Veh-treated conditions show fewer ontologies directly relevant to neuronal activity (Figure 4D; Table S4). RNA-Enrich provides the identity of signature genes, called Sig-genes, which contributed to the enrichment of an ontology (Kim et al., 2012; Lee et al., 2016). As expected, Sig-genes for the synapse-related ontologies, including *Ngf*, *Syn3*, *Cacna1b*, and *Rab3a*, showed mild yet reproducible transcriptional changes upon *Rai1* KD (Figure 4E; Figure S4B).

RAI1 Dissociates from Chromatin in Response to Activity Changes

The activity state-dependent requirement of RAI1 in regulating transcription led us to hypothesize that activity shifts of neuronal network might alter RAI1 distribution on chromatin. To test this, we performed chromatin immunoprecipitation coupled with deep sequencing (ChIP-seq) for RAI1 in DIV 17 neuronal cultures treated for 4 h with TTX, BIC, or vehicle. We observed clear RAI1 binding at the promoters of RAI1-dependent genes such as *Homer1* and *Per2* (Figure 5A). The control ChIP using *Rai1*-KD cultures showed no such events, demonstrating the specificity of ChIP experiments. RAI1 binding was much weaker in TTX- or BIC-treated cultures (Figure 5A). Consistent with visual observations, peak calling identified only 13 RAI1 peaks across all three *Rai1*-KD ChIP-seq samples (not shown), and they were removed from all subsequent analyses. In shCtrl cells, 6,065 RAI1 peaks were found in the Veh-treated condition, and a drastic reduction of RAI1 peaks upon TTX (98 peaks) and BIC (1 peak) treatments (Figure 5B). Variable ChIP efficiency or sequencing depth cannot explain the scarce peaks in TTX and BIC conditions, because we spiked in *Drosophila* chromatin and fly-specific H2Av antibody and ensured consistent sequencing depth and ChIP efficiency across the samples (Figure S5A). Neither RAI1 protein levels (Figure S5B) nor nuclear localization (Figure S2A) changed after TTX or BIC treatment. Thus, activity alterations largely release RAI1 from chromatin, which is remarkably consistent with the greater number of RAI1-dependent genes in resting neurons (Figure 4B).

RAI1 Directly Controls Activity-Responsive Gene Transcription in Stable Networks

Intersection with BrU-seq data revealed that that RAI1-bound genes are much more likely responsive to network activity shifts than RAI1-free genes ($p < 2.2 \times 10^{-16}$, chi-square test; Figure 5C;

Figure 4. RAI1 Positively Regulates the Transcriptional Response to TTX

(A) The fold changes of TTX- and BIC-response genes in cultures treated by sh-Ctrl or sh-*Rai1* (Wilcoxon rank-sum test). Whiskers represent 1.5 times IQR, and the notch represents the 95% confidence interval of the median.

(B) Number of DESeq2-called differentially expressed genes (sh-Ctrl versus sh-*Rai1*, $p_{adj} < 0.05$) after TTX, vehicle, or BIC treatment.

(C) Incomplete downregulation and upregulation of genes by TTX (left) but not by BIC (right) in *Rai1*-KD cultures. r and p, Spearman's rank correlation coefficient and p value.

(D) RAI1-dependent gene ontologies (biological process, $p_{adj} < 0.005$) discovered using RNA-Enrich (Lee et al., 2016) and filtered using ReviGO software (Supek et al., 2011).

(E) RPKM (reads per kilobase of transcript per million mapped reads) values of four Sig-genes downregulated by *Rai1* KD in the TTX-treated condition. The Sig-genes represent "neurotransmitter transport" ($p_{adj} = 9.3 \times 10^{-8}$), the top downregulated biological processes. The remaining Sig-genes are shown in Figure S7. Note slight but consistent inter-replicate changes upon *Rai1* KD.

See also Figure S4 and Tables S3 and S4.

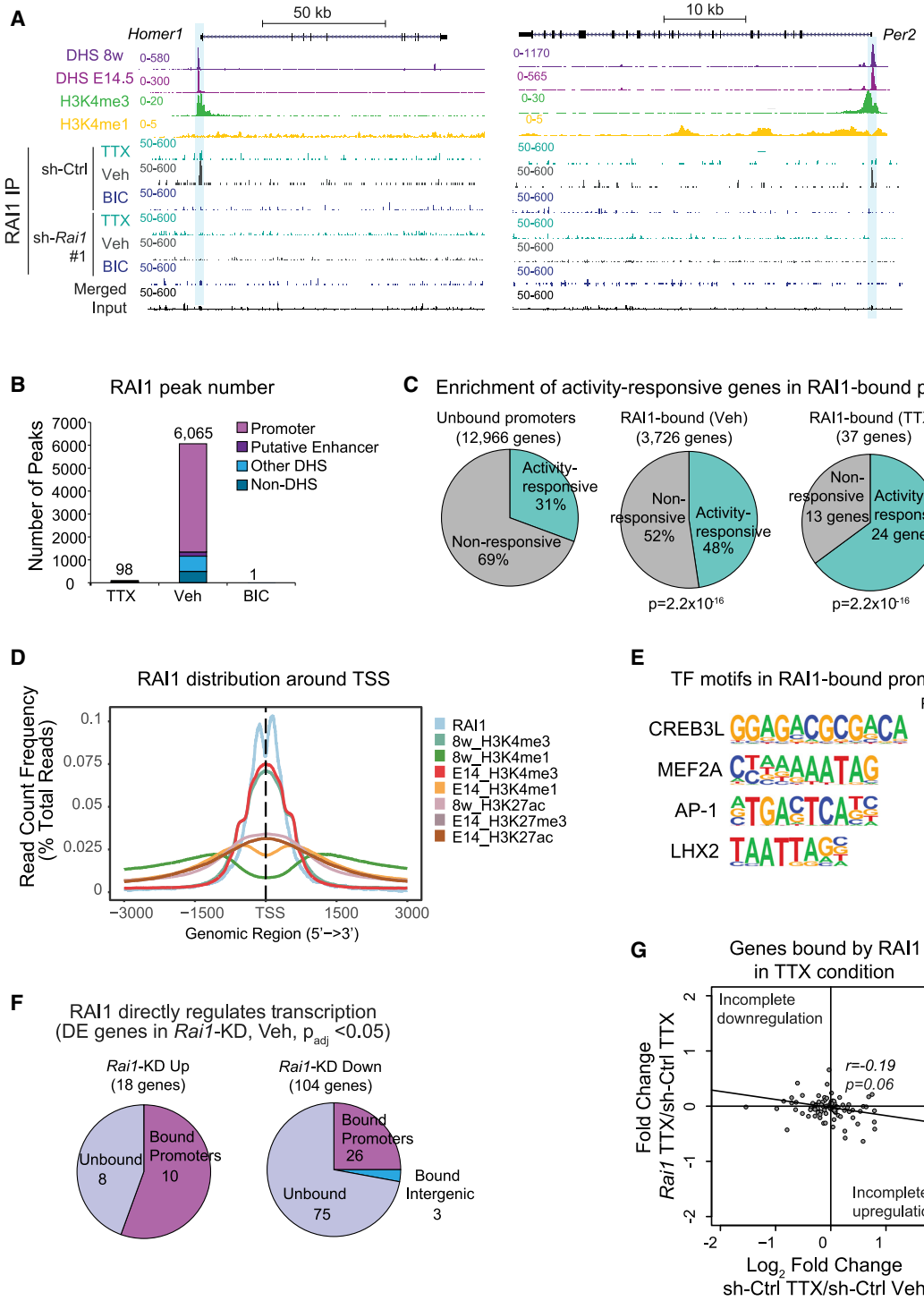

Figure 5. Activity-Dependent Chromatin Engagement of RAI1

(A) UCSC Browser view of RAI1 ChIP-seq signals at *Rai1*-dependent genes *Homer1* and *Per2*.

(B) Number of RAI1 peaks in TTX-, vehicle-, and BIC-treated cultures.

(C) RAI1-bound promoters are enriched for activity-response genes (chi-square test, $p = 2.2 \times 10^{-16}$).

(D) Bimodal RAI1 distribution around TSS. H3K4me3, H3K4me1, H3K27me3, and H3K27ac levels are plotted as controls (see STAR Methods).

(E) Activity-dependent TF motifs enriched in RAI1 peaks.

(F) RAI1 directly up- and downregulates transcription in the naive culture.

(G) RAI1-bound genes in the TTX condition show incomplete induction and suppression by TTX in *Rai1* KD cells.

See also Figure S5 and Table S5.

Figure S5C). Consistently, RAI1-bound genes associated with plasticity-related ontologies including synapse organization (Figure S5D). Most of these peaks are present at the promoters in the resting culture (Figure 5B) and exhibited a bimodal distribution around transcription start sites (TSSs) that harbor H3K4me3 (Figure 5D). Binding motifs of activity-dependent TFs (e.g., MEF2A, AP1, LHX2, CREB3L) are enriched in RAI1-bound promoters (Figure 5D). RAI1 also occupied intra- and intergenic regions. In the resting culture, 54% of such non-promoter regions overlapped with DNase-I hypersensitivity sites (DHSs) identified in 8-week-old mouse whole brain (Vierstra et al., 2014), and the rest were DHS free (Figure 5B). Some RAI1-bound DHS coincided with H3K4me1 or H3K27ac (Creyghton et al., 2010), indicating that these elements are likely transcriptional enhancers (Figure 5B; see STAR Methods). A substantial fraction (67%) of RAI1 peaks overlapped with previously reported RAI1 peaks in adult mouse brain (Huang et al., 2016) with common TF motifs (Figures S5E and S5F). In sum, these analyses show that RAI1 preferentially engages activity-responsive promoters with H3K4me3 in neural networks with stable basal levels of activity.

Are the RAI1-dependent genes found in BrU-seq direct targets of RAI1? Of the genes up- or downregulated by *Rai1* KD, RAI1 occupied 40 of 122 genes (30%) in the baseline culture, which is significantly higher than the genomic average ($p < 0.05$, chi-square test; Figure S5G). The direct targets of RAI1 can be up- or downregulated upon RAI1 loss (Table S5). Of the 18 genes upregulated by *Rai1* KD, RAI1 binds to 10 promoters (Figure 5F), while RAI1 occupies 29 of 104 genes downregulated by *Rai1* KD. These results support the idea that RAI1 uses both positive and negative regulation to repress the TTX-like transcription state in cultures with stable basal levels of activity (Figures 2B–2D). Of note, BIC-response genes, which show no dependence on RAI1, also showed RAI1 peak enrichment (Figure S5C); therefore, RAI1 at these genes is dispensable for suppressing BIC-triggered transcription.

RAI1 Directly Contributes to Transcriptional Response to TTX

Finally, we inspected the 98 RAI1 peaks found in TTX-treated cultures, because we detected a compromised transcriptional response of *Rai1*-KD cells to TTX (Figures 4C–4E). Most of these peaks were common between the TTX and vehicle conditions (promoter-occupied, 89% overlap; non-promoter-occupied, 77% overlap; Figure S5H). We found a much greater proportion of non-promoter peaks (60%) compared with the resting cells (22%) (Figure S5I). Thus, RAI1 at non-promoter regions preferentially persists when network activity decreases. The genes bound or nearest to these RAI1-TTX peaks showed incomplete induction and suppression upon TTX treatment of *Rai1*-KD cultures (Figure 5G) but not upon BIC treatment (Figure S5J). These results suggest that RAI1 directly contributes to the transcriptional response (both negative and positive) to TTX and that this role involves primarily non-promoter regulation.

Loss of RAI1 Prevents Synaptic Upscaling but Not Downscaling

We next examined RAI1's role in homeostatic synaptic scaling induced by chronic activity suppression (TTX, 24 h) or chronic network hyperactivation (BIC, 24 h). Consistent with the misregulation of TTX-responsive genes by *Rai1* KD after TTX treatment (Figures 4 and 5), we found that loss of RAI1 significantly impaired the induction of homeostatic upscaling during activity suppression in a cell-autonomous manner. Following transfection of scrambled or *Rai1*-targeted shRNAs (24 h prior to TTX/BIC), we found that control neurons expressing the scrambled shRNA exhibited the normal increase in mEPSC amplitude 24 h post-TTX (sh-Ctrl Veh versus TTX, n = 29-21, $p < 0.0001$; Figures 6A and 6B) and the distribution of mEPSCs exhibited a clear and multiplicative rightward shift in cumulative frequency plots. In contrast, mEPSCs from neurons expressing either of two distinct *Rai1* shRNAs did not significantly increase following TTX exposure (Figures 6A–6C). Importantly, expression of an RNAi-resistant RAI1 fully rescued TTX-induced upscaling (Figures 6A–6C). Despite a clear role in homeostatic upscaling, *Rai1* KD had no effect on the induction of homeostatic downscaling following network hyperactivation with BIC (Figures 6D–6F). Both control neurons expressing scrambled shRNA and those neurons expressing *Rai1* shRNA exhibited significantly decreased mEPSC amplitudes (sh-Ctrl Veh versus BIC, n = 26-17, $p = 0.0026$; sh-*Rai1*-#1 Veh versus BIC, n = 21-8, $p = 0.0003$; and sh-*Rai1*-#2 Veh versus BIC, n = 12-8, $p < 0.0001$; Figure 6E), as well as a clear leftward multiplicative shift in mEPSC cumulative probability distributions (Figure 6F). These results demonstrate that RAI is essential for homeostatic upscaling during activity suppression but is otherwise dispensable for homeostatic downscaling during periods of network hyperactivation.

Discussion

Our BrU-seq analysis has provided insights into activity-dependent transcriptional regulation. We found widespread transcriptional responses to network activity shifts attributable to BrU-seq's high sensitivity in detecting transcriptional downregulation. Most dynamically regulated genes altered by hyperactivity or suppression are unique rather than reciprocal (Figure 1). This is interesting given that gene expression studies have focused on reciprocal regulation of genes (e.g., *Arc*, *Fos*, *Homer1*, and *Bdnf*) (Okuno, 2011). Our results agree with a nascent proteome study on rat hippocampal neurons, in which the authors observed unique, common, and reciprocal changes in protein synthesis upon TTX and BIC treatments (Schanzenbächer et al., 2016). These observations suggest that besides the reciprocal transcriptional changes of key factors, distinct transcriptional mechanisms may underlie upscaling and downscaling. Our data therefore provide a resource to begin an exploration of such distinct molecular machineries.

Several lines of evidence support a model in which RAI1 acts to constrain synaptic upscaling in networks with baseline levels of activity by preventing premature transcriptional responses normally driven by altered network activity (Figure 7). First, RAI1 deficiency shifts gene expression toward TTX-associated transcriptional states (Figure 2). Second, RAI1 occupies its target promoters strongly in the resting cells and dissociates when network activity shifts (Figure 5). Third, *Rai1* KD led to an increase in excitatory synaptic strength, reflected by enhanced mEPSC amplitudes and associated with an increase in network firing rate (Figure 3). Our data further indicate the additional role of RAI1 in promoting synaptic upscaling when the network

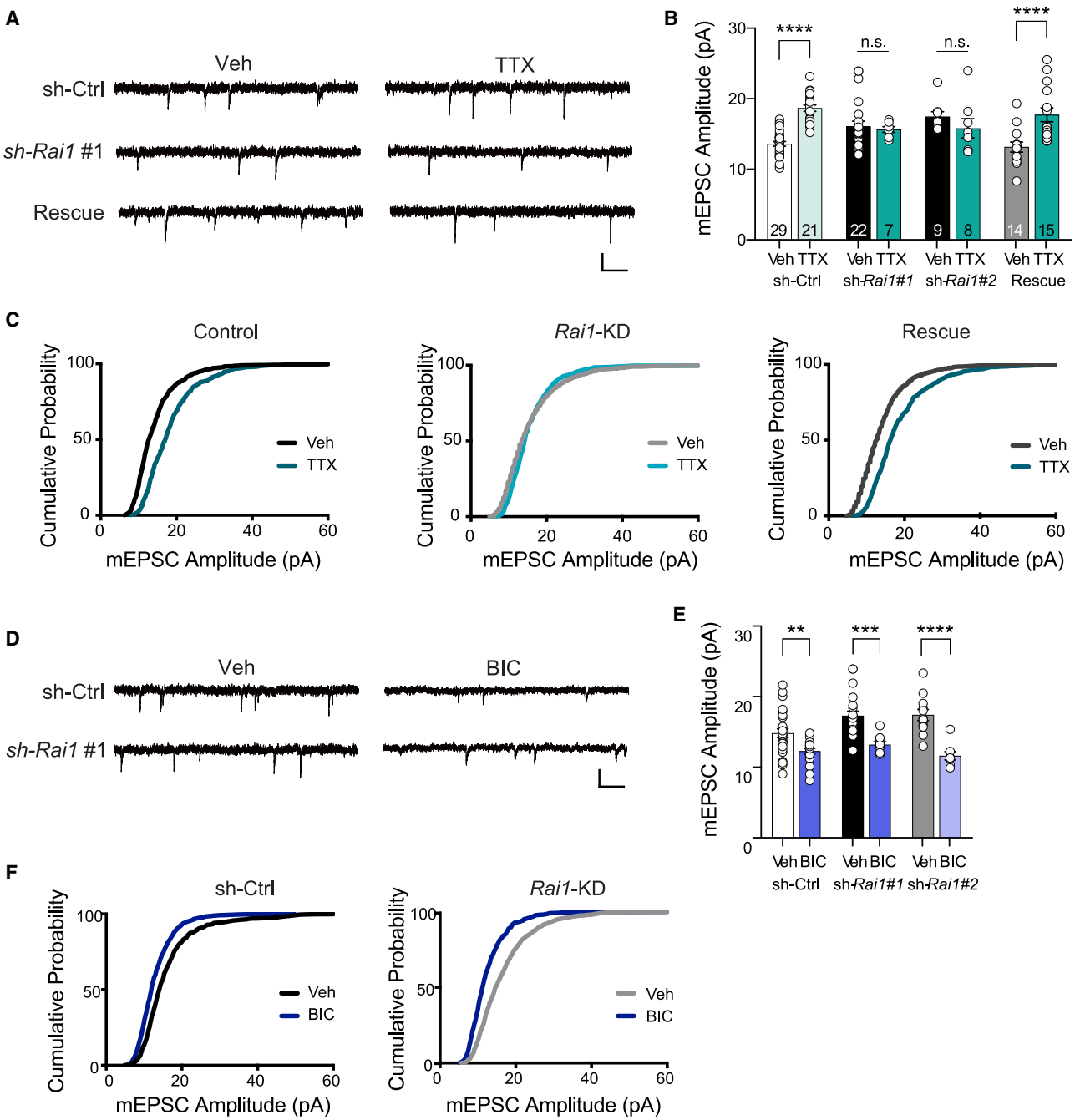

Figure 6. *Rai1* KD Impairs Synaptic Upscaling but Not Synaptic Downscaling

(A–C) Representative mEPSC traces recorded from neurons transfected with sh-Ctrl, sh-*Rai1*, or rescue and treated with either vehicle or 1 μM TTX. Scale bar, 20 pA, 150 ms.

(B) mEPSC amplitude of sh-Ctrl, sh-*Rai1* #1, sh-*Rai1* #2, or rescue and treated either with vehicle or TTX (sh-Ctrl Veh, TTX n = 29-21; sh-*Rai1* #1 Veh, TTX n = 22-7; sh-*Rai1* #2 Veh, TTX n = 9-8; and rescue Veh, TTX n = 14-15).

(C) Cumulative distribution of mEPSC amplitude for sh-Ctrl (left), *Rai1* KD (sh-*Rai1* #1 + #2, middle), and rescue (right) comparing vehicle versus TTX.

(D–F) Representative mEPSC traces recorded from neurons transfected with either sh-Ctrl or sh-*Rai1* and treated with either vehicle or 10 μM BIC (D). Scale bar, 20 pA, 150 ms. (E) mEPSC amplitude of sh-Ctrl, sh-*Rai1* #1, and sh-*Rai1* #2 treated either with vehicle or BIC (sh-Ctrl Veh, BIC n = 26-17; sh-*Rai1* #1 Veh, BIC n = 21-8; sh-*Rai1* #2 Veh, BIC n = 12-8). (F) Cumulative distribution of mEPSC amplitude of sh-Ctrl (left) and sh-*Rai1* (sh-*Rai1* #1 + #2) treated with vehicle (black) or BIC (blue).

All bar graphs are represented as mean ± SEM, and unpaired Student's t tests were performed. **p < 0.01, ***p < 0.001, and ****p < 0.0001.

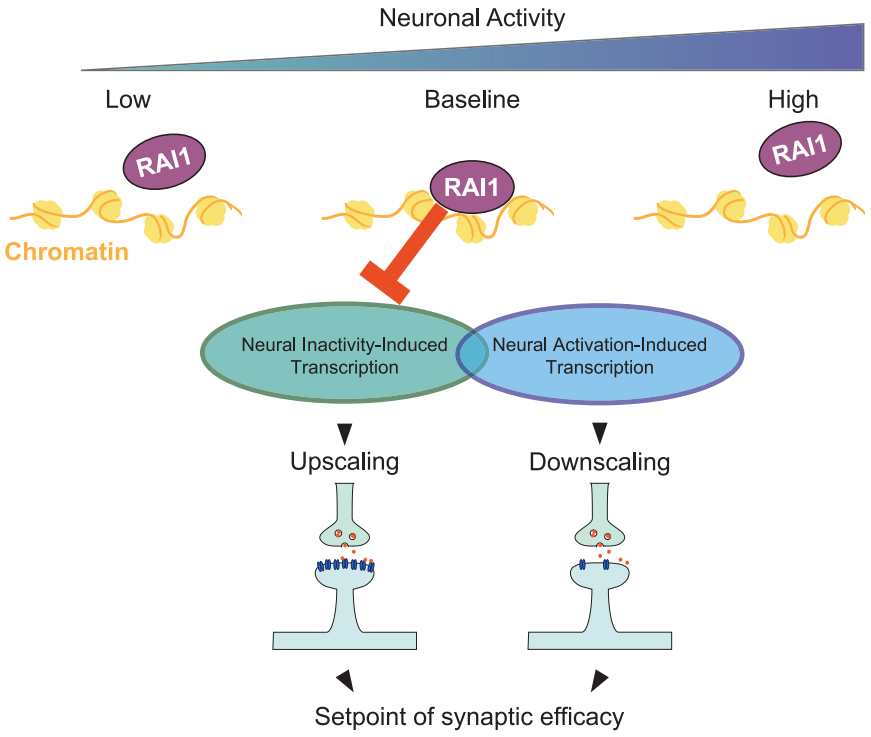

Figure 7. RAI1's Role as a State-Dependent Transcriptional Regulator of TTX-Response Genes

RAI1 alters synaptic efficacy through activity-dependent chromatin binding and plays essential roles in regulating TTX-response genes under baseline and activity-suppressed states.

experiences prolonged activity depression (Figure 6). This latter role of RAI1 again involves direct control of TTX-induced transcriptional responses (Figures 4 and 5). The most remarkable aspect of these observations might be the predictive capability of BrU-seq results for RAI1's roles in chromatin regulation and synaptic plasticity.

The present work provides insights into RAI1-mediated regulation of gene transcription. RAI1 is a nucleosome-binding protein and is thought to act as a transcriptional coactivator (Bi et al., 2005). Our data demonstrate that RAI1 can also repress transcription depending on the target genes (Figure 5). We could not identify genomic features that separate coactivator and corepressor functions (not shown), but other studies suggest some possibilities. Like RAI1, TET3 and EHMT1/2 have important roles in homeostatic upscaling (Benevento et al., 2016; Yu et al., 2015b). While TET3 positively regulates transcription by removing CpG methylation (Ito et al., 2010), EHMT1/2 generally acts as a transcriptional repressor by placing the repressive histone H3K9 methylation mark (Tachibana et al., 2005). Thus, the two facets of RAI1's role in transcriptional dynamics could be through interactions with positive and negative transcriptional regulators, such as TET3 and EHMT1/2.

It is noteworthy that all the four previously characterized chromatin regulators in synaptic scaling (i.e., TET3, EHMT1/2, and L3MBTL1) were chosen for investigations, because network activity alters their expression or target histone modifications (Benevento et al., 2016; Mao et al., 2018; Yu et al., 2015b). We found no indication that neuronal activity influences RAI1 expression (Figures S2A and S5B). These observations suggest that chromatin regulators linked to human cognitive disorders could participate in synaptic scaling and other forms of transcription-dependent plasticity, even when their expression remains stable during the process. The predominant chromatin occupancy by RAI1 during stable periods of network activity (Figure 5) is unique among the scaling-associated chromatin factors, which all appear to be activated by network activity alterations. Post-translational modifications on RAI1 itself or chromatin are potential mechanisms for the RAI1 dissociation from chromatin. Thus, RAI1 offers a molecular mechanism that stabilizes network activity, and future investigations may uncover a similar mode of action in other chromatin regulators associated with human cognitive deficits.

How do RAI1's roles in synaptic scaling relate to cognitive function? Thorough characterization of cell type-specific *Rai1*-KO mice attributed their learning deficits to GABAergic interneurons rather than glutamatergic excitatory neurons (Huang et al., 2016). Because we measured mEPSCs in the pyramidal cells that incorporated the sparsely transfected *Rai1*-shRNA plasmid, RAI1's role in synaptic scaling is cell autonomous to excitatory neurons. The lack of learning deficits in forebrain-specific *Rai1*-KO (*Emx1*-Cre: $Rai1^{flox/flox}$) may suggest that impaired cognitive function is independent of RAI1's role in synaptic scaling. Alternatively, unknown genes may compensate for synaptic scaling deficits during development thus obscuring the contribution of RAI1 in excitatory neurons that can only be seen in acute RAI1 deficiency. Of note, a recent study reported reduced dendritic spine density in the prefrontal cortex of 4-week-old *Rai1*-heterozygous mice (Huang et al., 2018), which are genetically similar to SMS patients. The spine deficits in *Rai1*-heterozygous mice may relate to RAI1's role in synaptic upscaling identified here. Identifying RAI1-target genes that mediate the synaptic phenotype will illuminate the molecular pathways underlying the cell-autonomous roles of RAI1.

A limitation of the BrU-seq approach is the lack of cell type specificity. Recently, Zajaczkowski et al. (2018) reported nascent RNA-seq specifically in neurons. They used *Synapsin I* promoter-driven expression of uracil phosphoribosyltransferase (UPRT) to label RNAs of neurons. The UPRT system identified more than 3,000 depolarization-regulated genes over the 3 h KCl treatments, which likely detected both nascent transcripts and steady-state mRNAs. Cell type specificity of the UPRT system comes with the cost of introducing the UPRT transgene and additional experimental steps to label RNAs. Furthermore, single-cell RNA-seq of *Rai1*-KD neurons might illuminate cell type-specific roles for RAI1.

Single-cell RNA-seq, however, mostly characterizes poly(A)-selected steady-state mRNAs. Thus, it will be important to choose the most suitable experimental approach for RNA profiling depending on specific goals of the study.

Our RAI1 ChIP-seq study involves a single replicate because of the unexpected and sustained laboratory closures during the ongoing coronavirus disease 2019 (COVID-19) pandemic. When laboratory operations resume, we plan to collect data of a second replicate and share the data via the GEO database. Our ChIP-seq data, nonetheless, include robust controls (i.e., *Rai1*-KD samples and internal spike-in controls); therefore, it is unlikely that the conclusion will change with new datasets.

In summary, our results indicate that nascent RNA-seq with BrU-seq uncovers robust and dynamic transcriptional responses during alterations in network activity. Transcriptional changes are largely unique in response to network hyperactivation or suppression, rather than reciprocal. Our studies further identify a unique role for RAI1 in homeostatic synaptic plasticity, whereby during stable patterns of activity, it suppresses a transcriptional program engaged during activity suppression. These findings illuminate principles whereby dysregulated chromatin signaling may contribute to neurodevelopmental disorders.

STAR★METHODS

Detailed methods are provided in the online version of this paper and include the following:

- KEY RESOURCES TABLE
- RESOURCE AVAILABILITY
  - Lead Contact
  - Materials Availability
  - Data and Code Availability
- EXPERIMENTAL MODEL AND SUBJECT DETAILS
  - Primary Mouse Forebrain Cultures
  - Primary Rat Hippocampal Cultures
- METHOD DETAILS
  - Lentivirus preparation
  - Activity Alteration and Bru-seq
  - ChIP-seq
  - Patch-Clamp Electrophysiology
  - Multi-Electrode Array Electrophysiology
  - Immunofluorescence
  - Western Blot
- QUANTIFICATION AND STATISTICAL ANALYSIS
  - Bru-seq Activity-Induction
  - ChIP-seq
  - Patch-Clamp Electrophysiology
  - Multi-Electrode Array Electrophysiology
  - Immunofluorescence
  - Western blot

SUPPLEMENTAL INFORMATION

Supplemental Information can be found online at https://doi.org/10.1016/j.celrep.2020.108002.

ACKNOWLEDGMENTS

We thank Dr. Saurabh Agarwal for providing technical support for BrU-seq experiments and scripts for mapping and annotating RNA-seq data. We thank Yu (Celine) Chuo for technical support in experiments and helpful discussion. We thank the Smrcka lab for neonatal rat tissue. P.M.G. was supported by a National Science Foundation (NSF) Graduate Research Fellowship Program (DGE #1256260). T.T. was supported by a Parents and Researchers Interested in Smith-Magenis Syndrome (PRISMS) post-doctoral fellowship. A.C. was supported by a National Institutes of Health (NIH) National Research Service Award (NRSA) fellowship (18-PAF03228). M.A.W. was supported by a Summer Fellowship from the University of Michigan Language, Sciences, and Arts Honors Program. This work was supported by the University of Michigan Medical School (to S.I.), the March of Dimes Foundation (to S.I.), and the NIH (R01DA020140 to K.S.J.; R01NS089896, R01NS116008, and R21NS104774 to S.I.; R01NS097498 to M.A.S.). We thank the members of Iwase and Sutton laboratories for discussion and support.

AUTHOR CONTRIBUTIONS

Conceptualization, P.M.G., M.A.S., and S.I.; Methodology, P.M.G., T.T., S.I., M.A.S., J.C.R.D., K.S.J., and R.K.; Validation, P.M.G., A.C., T.T., J.C.R.D., R.K., J.C.A., and M.A.W.; Formal Analysis, P.M.G., A.C., T.T., J.C.R.D., R.K., M.A.S., J.C.A., and M.A.W.; Investigation, P.M.G., A.C., T.T., J.C.R.D., R.K., J.C.A., and M.A.W.; Resources, R.J.G., K.S.J., M.A.S., and S.I.; Data Curation, P.M.G., A.C., T.T., J.C.R.D., R.K., and M.A.W.; Writing—Original Draft, P.M.G., A.C., T.T., J.C.R.D., K.S.J., M.A.S., and S.I.; Writing—Review & Editing: P.M.G., A.C., T.T., J.C.R.D., R.K., M.A.W., R.J.G., K.S.J., M.A.S., and S.I.; Visualization, P.M.G., A.C., T.T., J.C.R.D., R.K., and M.A.W.; Supervision, P.M.G., M.A.S., and S.I.; Project Administration, P.M.G., T.T., M.A.S., and S.I.; Funding Acquisition, P.M.G., T.T., R.J.G., K.S.J., M.A.S., and S.I.

DECLARATION OF INTERESTS

The authors declare no competing interests.

Received: January 29, 2019
Revised: June 17, 2020
Accepted: July 15, 2020
Published: August 11, 2020

REFERENCES

Abbott, L.F., and Nelson, S.B. (2000). Synaptic plasticity: taming the beast. Nat. Neurosci. *3* (*Suppl*), 1178–1183.

Bateup, H.S., Johnson, C.A., Denefrio, C.L., Saulnier, J.L., Kornacker, K., and Sabatini, B.L. (2013). Excitatory/inhibitory synaptic imbalance leads to hippocampal hyperexcitability in mouse models of tuberous sclerosis. Neuron *78*, 510–522.

Benevento, M., Iacono, G., Selten, M., Ba, W., Oudakker, A., Frega, M., Keller, J., Mancini, R., Lewerissa, E., Kleefstra, T., et al. (2016). Histone methylation by the Kleefstra syndrome protein EHMT1 mediates homeostatic synaptic scaling. Neuron *91*, 341–355.

Benito, E., and Barco, A. (2015). The neuronal activity-driven transcriptome. Mol. Neurobiol. *51*, 1071–1088.

Bi, W., Saifi, G.M., Shaw, C.J., Walz, K., Fonseca, P., Wilson, M., Potocki, L., and Lupski, J.R. (2004). Mutations of RAI1, a PHD-containing protein, in non-deletion patients with Smith-Magenis syndrome. Hum. Genet. *115*, 515–524.

Bi, W., Ohyama, T., Nakamura, H., Yan, J., Visvanathan, J., Justice, M.J., and Lupski, J.R. (2005). Inactivation of Rai1 in mice recapitulates phenotypes observed in chromosome engineered mouse models for Smith-Magenis syndrome. Hum. Mol. Genet. *14*, 983–995.

Bi, W., Yan, J., Shi, X., Yuva-Paylor, L.A., Antalffy, B.A., Goldman, A., Yoo, J.W., Noebels, J.L., Armstrong, D.L., Paylor, R., and Lupski, J.R. (2007). Rai1 deficiency in mice causes learning impairment and motor dysfunction,

whereas Rai1 heterozygous mice display minimal behavioral phenotypes. Hum. Mol. Genet. *16*, 1802–1813.

Bourgeron, T. (2015). From the genetic architecture to synaptic plasticity in autism spectrum disorder. Nat. Rev. Neurosci. *16*, 551–563.

Boxer, L.D., Renthal, W., Greben, A.W., Whitwam, T., Silberfeld, A., Stroud, H., Li, E., Yang, M.G., Kinde, B., Griffith, E.C., et al. (2020). MeCP2 Represses the rate of transcriptional initiation of highly methylated long genes. Mol. Cell *77*, 294–309.e9.

Brakeman, P.R., Lanahan, A.A., O'Brien, R., Roche, K., Barnes, C.A., Huganir, R.L., and Worley, P.F. (1997). Homer: a protein that selectively binds metabotropic glutamate receptors. Nature *386*, 284–288.

Bramham, C.R., Worley, P.F., Moore, M.J., and Guzowski, J.F. (2008). The immediate early gene arc/arg3.1: regulation, mechanisms, and function. J. Neurosci. *28*, 11760–11767.

Campbell, R.R., and Wood, M.A. (2019). How the epigenome integrates information and reshapes the synapse. Nat. Rev. Neurosci. *20*, 133–147.

Creyghton, M.P., Cheng, A.W., Welstead, G.G., Kooistra, T., Carey, B.W., Steine, E.J., Hanna, J., Lodato, M.A., Frampton, G.M., Sharp, P.A., et al. (2010). Histone H3K27ac separates active from poised enhancers and predicts developmental state. Proc. Natl. Acad. Sci. U S A *107*, 21931–21936.

Darvekar, S., Johnsen, S.S., Eriksen, A.B., Johansen, T., and Sjøttem, E. (2012). Identification of two independent nucleosome-binding domains in the transcriptional co-activator SPBP. Biochem. J. *442*, 65–75.

Darvekar, S., Rekdal, C., Johansen, T., and Sjøttem, E. (2013). A phylogenetic study of SPBP and RAI1: evolutionary conservation of chromatin binding modules. PLoS ONE *8*, e78907.

Ebert, D.H., and Greenberg, M.E. (2013). Activity-dependent neuronal signalling and autism spectrum disorder. Nature *493*, 327–337.

Egan, B., Yuan, C.C., Craske, M.L., Labhart, P., Guler, G.D., Arnott, D., Maile, T.M., Busby, J., Henry, C., Kelly, T.K., et al. (2016). An alternative approach to ChIP-seq normalization enables detection of genome-wide changes in histone H3 lysine 27 trimethylation upon EZH2 inhibition. PLoS ONE *11*, e0166438.

Elsea, S.H., and Williams, S.R. (2011). Smith-Magenis syndrome: haploinsufficiency of RAI1 results in altered gene regulation in neurological and metabolic pathways. Expert Rev. Mol. Med. *13*, e14.

ENCODE Project Consortium (2012). An integrated encyclopedia of DNA elements in the human genome. Nature *489*, 57–74.

Fernandes, D., and Carvalho, A.L. (2016). Mechanisms of homeostatic plasticity in the excitatory synapse. J. Neurochem. *139*, 973–996.

Fragoso, Y.D., Stoney, P.N., Shearer, K.D., Sementilli, A., Nanescu, S.E., Sementilli, P., and McCaffery, P. (2014). Expression in the human brain of retinoic acid induced 1, a protein associated with neurobehavioural disorders. Brain Struct. Funct. *220*, 1195–1203.

Girirajan, S., Elsas, L.J., 2nd, Devriendt, K., and Elsea, S.H. (2005). RAI1 variations in Smith-Magenis syndrome patients without 17p11.2 deletions. J. Med. Genet. *42*, 820–828.

Glock, C., Heumüller, M., and Schuman, E.M. (2017). mRNA transport & local translation in neurons. Curr. Opin. Neurobiol. *45*, 169–177.

Guzman-Karlsson, M.C., Meadows, J.P., Gavin, C.F., Hablitz, J.J., and Sweatt, J.D. (2014). Transcriptional and epigenetic regulation of Hebbian and non-Hebbian plasticity. Neuropharmacology *80*, 3–17.

Hasel, P., Dando, O., Jiwaji, Z., Baxter, P., Todd, A.C., Heron, S., Márkus, N.M., McQueen, J., Hampton, D.W., Torvell, M., et al. (2017). Neurons and neuronal activity control gene expression in astrocytes to regulate their development and metabolism. Nat. Commun. *8*, 15132.

Henry, F.E., McCartney, A.J., Neely, R., Perez, A.S., Carruthers, C.J.L., Stuenkel, E.L., Inoki, K., and Sutton, M.A. (2012). Retrograde changes in presynaptic function driven by dendritic mTORC1. J. Neurosci. *32*, 17128–17142.

Hermey, G., Blüthgen, N., and Kuhl, D. (2017). Neuronal activity-regulated alternative mRNA splicing. Int. J. Biochem. Cell Biol. *91* (*Pt B*), 184–193.

Hrvatin, S., Hochbaum, D.R., Nagy, M.A., Cicconet, M., Robertson, K., Cheadle, L., Zilionis, R., Ratner, A., Borges-Monroy, R., Klein, A.M., et al. (2018). Single-cell analysis of experience-dependent transcriptomic states in the mouse visual cortex. Nat. Neurosci. *21*, 120–129.

Huang, W.H., Guenthner, C.J., Xu, J., Nguyen, T., Schwarz, L.A., Wilkinson, A.W., Gozani, O., Chang, H.Y., Shamloo, M., and Luo, L. (2016). Molecular and neural functions of Rai1, the causal gene for Smith-Magenis syndrome. Neuron *92*, 392–406.

Huang, W.-H., Wang, D.C., Allen, W.E., Klope, M., Hu, H., Shamloo, M., and Luo, L. (2018). Early adolescent Rai1 reactivation reverses transcriptional and social interaction deficits in a mouse model of Smith-Magenis syndrome. Proc. Natl. Acad. Sci. U S A *115*, 10744–10749.

Ibata, K., Sun, Q., and Turrigiano, G.G. (2008). Rapid synaptic scaling induced by changes in postsynaptic firing. Neuron *57*, 819–826.

Igaz, L.M., Vianna, M.R.M., Medina, J.H., and Izquierdo, I. (2002). Two time periods of hippocampal mRNA synthesis are required for memory consolidation of fear-motivated learning. J. Neurosci. *22*, 6781–6789.

Ito, S., D'Alessio, A.C., Taranova, O.V., Hong, K., Sowers, L.C., and Zhang, Y. (2010). Role of Tet proteins in 5mC to 5hmC conversion, ES-cell self-renewal and inner cell mass specification. Nature *466*, 1129–1133.

Iwase, S., Brookes, E., Agarwal, S., Badeaux, A.I., Ito, H., Vallianatos, C.N., Tomassy, G.S., Kasza, T., Lin, G., Thompson, A., et al. (2016). A mouse model of X-linked intellectual disability associated with impaired removal of histone methylation. Cell Rep. *14*, 1000–1009.

Kim, J.H., Karnovsky, A., Mahavisno, V., Weymouth, T., Pande, M., Dolinoy, D.C., Rozek, L.S., and Sartor, M.A. (2012). LRpath analysis reveals common pathways dysregulated via DNA methylation across cancer types. BMC Genomics *13*, 526.

Kim, D., Pertea, G., Trapnell, C., Pimentel, H., Kelley, R., and Salzberg, S.L. (2013). TopHat2: accurate alignment of transcriptomes in the presence of insertions, deletions and gene fusions. Genome Biol. *14*, R36.

Lacaria, M., Gu, W., and Lupski, J.R. (2013). Circadian abnormalities in mouse models of Smith-Magenis syndrome: evidence for involvement of RAI1. Am. J. Med. Genet. A. *161A*, 1561–1568.

Langmead, B., and Salzberg, S.L. (2012). Fast gapped-read alignment with Bowtie 2. Nat. Methods *9*, 357–359.

Langmead, B., Trapnell, C., Pop, M., and Salzberg, S.L. (2009). Ultrafast and memory-efficient alignment of short DNA sequences to the human genome. Genome Biol. *10*, R25.

Lee, C., Patil, S., and Sartor, M.A. (2016). RNA-Enrich: a cut-off free functional enrichment testing method for RNA-seq with improved detection power. Bioinformatics *32*, 1100–1102.

Liao, Y., Smyth, G.K., and Shi, W. (2014). featureCounts: an efficient general purpose program for assigning sequence reads to genomic features. Bioinformatics *30*, 923–930.

Love, M.I., Huber, W., and Anders, S. (2014). Moderated estimation of fold change and dispersion for RNA-seq data with DESeq2. Genome Biol. *15*, 550.

Mao, W., Salzberg, A.C., Uchigashima, M., Hasegawa, Y., Hock, H., Watanabe, M., Akbarian, S., Kawasawa, Y.I., and Futai, K. (2018). Activity-induced regulation of synaptic strength through the chromatin reader L3mbtl1. Cell Rep. *23*, 3209–3222.

Miller, K.D., and MacKay, D.J.C. (1994). The role of constraints in Hebbian learning. Neural Comput. *6*, 100–126.

Mullins, C., Fishell, G., and Tsien, R.W. (2016). Unifying views of autism spectrum disorders: a consideration of autoregulatory feedback loops. Neuron *89*, 1131–1156.

Okuno, H. (2011). Regulation and function of immediate-early genes in the brain: beyond neuronal activity markers. Neurosci. Res. *69*, 175–186.

Orlando, D.A., Chen, M.W., Brown, V.E., Solanki, S., Choi, Y.J., Olson, E.R., Fritz, C.C., Bradner, J.E., and Guenther, M.G. (2014). Quantitative ChIP-seq normalization reveals global modulation of the epigenome. Cell Rep. *9*, 1163–1170.

Paulsen, M.T., Veloso, A., Prasad, J., Bedi, K., Ljungman, E.A., Tsan, Y.-C., Chang, C.-W., Tarrier, B., Washburn, J.G., Lyons, R., et al. (2013). Coordinated

regulation of synthesis and stability of RNA during the acute TNF-induced proinflammatory response. Proc. Natl. Acad. Sci. U S A *110*, 2240–2245.

Paulsen, M.T., Veloso, A., Prasad, J., Bedi, K., Ljungman, E.A., Magnuson, B., Wilson, T.E., and Ljungman, M. (2014). Use of Bru-seq and BruChase-seq for genome-wide assessment of the synthesis and stability of RNA. Methods *67*, 45–54.

Potocki, L., Bi, W., Treadwell-Deering, D., Carvalho, C.M., Eifert, A., Friedman, E.M., Glaze, D., Krull, K., Lee, J.A., Lewis, R.A., et al. (2007). Characterization of Potocki-Lupski syndrome (dup(17)(p11.2p11.2)) and delineation of a dosage-sensitive critical interval that can convey an autism phenotype. Am. J. Hum. Genet. *80*, 633–649.

Risher, W.C., and Eroglu, C. (2012). Thrombospondins as key regulators of synaptogenesis in the central nervous system. Matrix Biol. *31*, 170–177.

Schanzenbächer, C.T., Sambandan, S., Langer, J.D., and Schuman, E.M. (2016). Nascent proteome remodeling following homeostatic scaling at hippocampal synapses. Neuron *92*, 358–371.

Schaukowitch, K., Reese, A.L., Kim, S.K., Kilaru, G., Joo, J.Y., Kavalali, E.T., and Kim, T.K. (2017). An intrinsic transcriptional program underlying synaptic scaling during activity suppression. Cell Rep. *18*, 1512–1526.

Slager, R.E., Newton, T.L., Vlangos, C.N., Finucane, B., and Elsea, S.H. (2003). Mutations in RAI1 associated with Smith-Magenis syndrome. Nat. Genet. *33*, 466–468.

Soden, M.E., and Chen, L. (2010). Fragile X protein FMRP is required for homeostatic plasticity and regulation of synaptic strength by retinoic acid. J. Neurosci. *30*, 16910–16921.

Supek, F., Bošnjak, M., Škunca, N., and Šmuc, T. (2011). REVIGO summarizes and visualizes long lists of gene ontology terms. PLoS ONE *6*, e21800.

Tachibana, M., Ueda, J., Fukuda, M., Takeda, N., Ohta, T., Iwanari, H., Sakihama, T., Kodama, T., Hamakubo, T., and Shinkai, Y. (2005). Histone methyltransferases G9a and GLP form heteromeric complexes and are both crucial for methylation of euchromatin at H3-K9. Genes Dev. *19*, 815–826.

Turrigiano, G.G. (2008). The self-tuning neuron: synaptic scaling of excitatory synapses. Cell *135*, 422–435.

Turrigiano, G.G. (2017). The dialectic of Hebb and homeostasis. Philos. Trans. R. Soc. Lond. B Biol. Sci. *372*, 20160258.

Vallianatos, C.N., Farrehi, C., Friez, M.J., Burmeister, M., Keegan, C.E., and Iwase, S. (2018). Altered gene-regulatory function of KDM5C by a novel mutation associated with autism and intellectual disability. Front. Mol. Neurosci. *11*, 104.

Vierstra, J., Rynes, E., Sandstrom, R., Zhang, M., Canfield, T., Hansen, R.S., Stehling-Sun, S., Sabo, P.J., Byron, R., Humbert, R., et al. (2014). Mouse regulatory DNA landscapes reveal global principles of cis-regulatory evolution. Science *346*, 1007–1012.

West, A.E., Griffith, E.C., and Greenberg, M.E. (2002). Regulation of transcription factors by neuronal activity. Nat. Rev. Neurosci. *3*, 921–931.

Widagdo, J., and Anggono, V. (2018). The m6A-epitranscriptomic signature in neurobiology: from neurodevelopment to brain plasticity. J. Neurochem. *147*, 137–152.

Yee, A.X., Hsu, Y.-T., and Chen, L. (2017). A metaplasticity view of the interaction between homeostatic and Hebbian plasticity. Philos. Trans. R. Soc. Lond. B Biol. Sci. *372*, 20160155.

Yu, G., Wang, L.G., and He, Q.Y. (2015a). ChIPseeker: an R/Bioconductor package for ChIP peak annotation, comparison and visualization. Bioinformatics *31*, 2382–2383.

Yu, H., Su, Y., Shin, J., Zhong, C., Guo, J.U., Weng, Y.-I., Gao, F., Geschwind, D.H., Coppola, G., Ming, G.-l., et al. (2015b). Tet3 regulates synaptic transmission and homeostatic plasticity via DNA oxidation and repair. Nat. Neurosci. *18*, 836–843.

Zajaczkowski, E.L., Zhao, Q.-Y., Zhang, Z.H., Li, X., Wei, W., Marshall, P.R., Leighton, L.J., Nainar, S., Feng, C., Spitale, R.C., and Bredy, T.W. (2018). Bioorthogonal metabolic labeling of nascent RNA in neurons improves the sensitivity of transcriptome-wide profiling. ACS Chem. Neurosci. *9*, 1858–1865.

Zhang, Y., Liu, T., Meyer, C.A., Eeckhoute, J., Johnson, D.S., Bernstein, B.E., Nusbaum, C., Myers, R.M., Brown, M., Li, W., and Liu, X.S. (2008). Model-based analysis of ChIP-seq (MACS). Genome Biol. *9*, R137.

Zhang, Y., Chen, K., Sloan, S.A., Bennett, M.L., Scholze, A.R., O'Keeffe, S., Phatnani, H.P., Guarnieri, P., Caneda, C., Ruderisch, N., et al. (2014). An RNA-sequencing transcriptome and splicing database of glia, neurons, and vascular cells of the cerebral cortex. J. Neurosci. *34*, 11929–11947.

Zhong, X., Li, H., and Chang, Q. (2012). MeCP2 phosphorylation is required for modulating synaptic scaling through mGluR5. J. Neurosci. *32*, 12841–12847.

STAR★METHODS

KEY RESOURCES TABLE

REAGENT or RESOURCE	SOURCE	IDENTIFIER
Antibodies		
anti-BrdU antibody	Santa Cruz Biotechnology	Cat. No. sc-32323; RRID: AB_626766
anti-PCNA antibody	Santa Cruz Biotechnology	Cat. No. sc-56; RRID: AB_628110
anti-beta-actin antibody	Sigma	Cat. No. A5441; RRID: AB_476744
HRP-conjugated secondary anti-IGG antibody	EMD Millipore	Cat. No. AP132P/Cat. No. AQ160P; RRID: AB_90264; RRID: AB_92795
anti-NeuN	EMD Millipore	Cat. No. MAB377; RRID: AB_2298772
anti-GFAP	NeuroMab	Cat. No. N206A/8; RRID: AB_10672298
anti-MAP2	EMD Millipore	Cat. No. AB5543; RRID: AB_571049
anti-OLIG2	EMD Millipore	Cat. No. AB9610; RRID: AB_570666
anti-CD11b	Abcam	Cat. No. ab133357; RRID: AB_2650514
anti-GAD67	Santa Cruz	Cat. No. sc-5602; RRID: AB_2107748
anti-GluA1	EMD Millipore	Cat. No. ABN241; RRID: AB_2721164
anti-PSD95	EMD Millipore	Cat. No. MAB1596; RRID: AB_2092365
Bacterial and Virus Strains		
pMD.2G plasmid for lentiviral production	AddGene	Plasmid #12259; RRID: Addgene_12259
psPAX2 plasmid for lentiviral production	AddGene	Plasmid #12260; RRID: Addgene_12260
Chemicals, Peptides, and Recombinant Proteins		
5-Bromouridine	Sigma	Cat. No. 18670
bicuculline-methiodide	Abcam	Cat. No. ab120108
Tri-Reagent BD	Sigma	Cat. No. T3809
DNase I	New England Biolabs	Cat. No. M0303
RNA ligase 1	New England Biolabs	Cat. No. M0437
truncated RNA ligase KQ	New England Biolabs	Cat. No. M0373
Deposited Data		
RAI1 Bru-seq/ChIP-seq data	Gene Expression Omnibus	GEO: GSE121749
DNase-Hypersensitivity sites, Mouse brain E14.5	Vierstra et al. (2014)	GEO: GSM1014197
DNase-Hypersensitivity sites, Mouse brain 8 week adult	Vierstra et al. (2014)	GEO: GSM1014151
H3K4me1 ChIp-seq, mouse brain, 8 week	ENCODE Project Consortium (2012)	GEO: GSM769022
H3K4me1 ChIp-seq, mouse brain, E14.5	ENCODE Project Consortium (2012)	GEO: GSM1000096
H3K4me3 ChIP-seq, mouse brain, 8 week	ENCODE Project Consortium (2012)	GEO: GSM769026
H3K4me3 ChIP-seq, mouse brain, E14.5	ENCODE Project Consortium (2012)	GEO: GSM1000095
H3K27ac ChIP-seq mouse brain, E14.5	ENCODE Project Consortium (2012)	GEO: GSM1000094
H3K27ac ChIP-seq mouse brain 8 week	Boxer et al. (2020)	GEO: GSM3666438
H3K27me2 ChIP-seq mouse brain E14.5	ENCODE Project Consortium (2012)	GEO: GSM1000143
H3K27me3 ChIP-seq mouse brain, 8 week	Boxer et al. (2020)	GEO: GSM3666437
Experimental Models: Organisms/Strains		
Mouse:CD-1	Charles River	Strain 022
Rat:Sprague-Dawley	Charles River	Strain 001
Oligonucleotides		
RNA-sequencing library preparation primers	See Table S6 for primers used	N/A

(*Continued on next page*)

Continued

REAGENT or RESOURCE	SOURCE	IDENTIFIER
Recombinant DNA		
full-length human RAI1 cDNA	reverse transcription from human cell lines	GenBank: NM_030665.3
Software and Algorithms		
Bowtie1	Langmead et al. (2009)	N/A
Bowtie2	Langmead and Salzberg (2012)	N/A
We used MACS2	Zhang et al. (2008)	version 2.1.0.20140616
DESeq2	Love et al. (2014)	N/A
Tophat2	Kim et al. (2013)	N/A
LRPath/RNAEnrich	Kim et al. (2012)	N/A
Custom MEA analysis	https://github.com/Jcrd25/NeuroMEACode	N/A

RESOURCE AVAILABILITY

Lead Contact

Further information and requests for resources and reagents should be directed to and will be fulfilled by Shigeki Iwase (siwase@umich.edu)

Materials Availability

There are restrictions to the availability of the custom RAI1 antibody due to limited supply.

Data and Code Availability

Sequencing data generated for this study have been submitted to the NCBI Gene Expression Omnibus (GEO; https://www.ncbi.nlm.nih.gov/geo/) under accession number GSE121749.

Custom MEA analysis scripts can be found at https://github.com/Jcrd25/NeuroMEACode

EXPERIMENTAL MODEL AND SUBJECT DETAILS

Primary Mouse Forebrain Cultures

Cortices and hippocampi from E18.5 CD1 mouse pups (Charles River, Strain 022) were pooled into biological replicates with identical female:male ratios. Sex of the pups was determined by PCR using primers for the ZFY gene (Table S6). Primary culture of neurons was carried out as previously described (Iwase et al., 2016; Vallianatos et al., 2018). Briefly, dissociated tissues were plated at 4 million cells/6 cm poly-D-lysine-coated plate (Sigma) grown in Neurobasal Media supplemented with B27 (GIBCO, #17504044). No mitotic inhibitors or antibiotics were added. Half the culture medium was freshened every 3-5 days.

Primary Rat Hippocampal Cultures

All animal use followed NIH guidelines and was in compliance with the University of Michigan Committee on Use and Care of Animals. Dissociated postnatal (P0-3) hippocampal neuron cultures were prepared from Sprague-Dawley rats (Charles River, Strain 001) as previously described (Henry et al., 2012). Sex of rat pups was not determined. For MEA experiments, neurons were plated onto sterile multi-electrode arrays chips (MEAs) (60MEA200/30IR–TI; Multichannel Systems, Reutlingen, Germany) at a density of ~350 cells/mm2. MEAs were coated with 0.05% polyethyleneimine and laminin (1 ug/ul). MEAs were transferred to the incubator for > 3 h to allow for cell adhesion. Media was composed of Neurobasal Plus Medium with 1X B-27 Plus supplement, 1X GlutaMax and 50 U/ml of Pen/Strep (ThermoFisher, Waltham, MA). MEAs were covered with a gas permeable ethlylene propylene membrane (MEA-MEM, Multichannel Systems, Reutlingen, Germany). Half-volume media exchanges were done every 3-4 days. Cultures that exhibited spontaneous spiking activity on ≥ 10 electrodes on DIV10 were considered healthy and included in the study.

METHOD DETAILS

Lentivirus preparation

Lentivirus were generated using co-transfection into HEK293t cells of psPAX2 (Addgene, 12260), pMD2.G (AddGene, 12259) and pLKO plasmids containing shRNA against *Rai1* untranslated region (*Rai1*-shRNA #1: Sigma, TRCN0000124984) or coding region (*Rai1*-shRNA #2: Sigma, TRCN0000328334) or scramble shRNA (Sigma, SHC202). For Bru-seq and ChIP-seq experiments, we used SHC202 and *Rai1*-shRNA #1. For electrophysiology, we used SHC202, *Rai1*-shRNA #1 and #2, whose target sequences are

identical between mouse and rat. The conditioned media containing lentiviruses was collected, concentrated with Lenti-X concentrator (Takara, 631232), and resuspended in Neurobasal medium, and stored at −80°C. The titer of lentivirus was determined by survival of transduced 293 cells under puromycin and a comparable amount of virus that result in >90% survival of infected neurons was used for all biological replicates.

Activity Alteration and Bru-seq

On DIV14, cells were infected with lentiviral shRNA as previously described (Vallianatos et al., 2018). On DIV17, cells were treated with bicuculline-methiodide (Abcam, ab120108, 20 μM), TTX (Tocris, 1069, 1 μM), or vehicle (sterile water), for 4 h. 3 h, and 40 min post treatment, bromouridine (Bru, Sigma, 18670, dissolved in PBS) was added to cultures at 2 mM final concentration. Cultures were harvested in Tri-reagent BD (Sigma, T3809) and frozen immediately. RNA was purified using phenol-chloroform extraction and isopropaonol precipitation, treated with DNase-I (NEB, M0303) then fragmented by high-magnesium, high temperature incubation. From 1 μg of total RNA, enrichment of Bru-containing RNA and library preparation were performed as previously described (Paulsen et al., 2013, 2014) with minor modifications. We designed custom adaptors (Table S6) which were directly ligated to the 3′ ends of RNA using RNA ligase 1 (NEB Cat. No. M0437) and truncated RNA ligase KQ (NEB M0373). Bromouridine-labeled RNAs were immunoprecipitated using anti-BrdU antibody (Santa Cruz Biotechnology, sc-32323). Enriched RNAs were reverse transcribed using a primer complementary to the RNA adaptor (Table S6). Adaptor duplexes with 5- or 6-base pair random nucleotide overhangs were ligated to the 3′ end of the cDNA (Table S6). The cDNA libraries were amplified using primers that carry Illumina indices, then 180-400 bp DNA fragments were isolated using by an agarose gel. The nucleotide sequences of primers used for library amplification are found in Table S6. The libraries were subjected to single-end 50-bp sequencing using Illumina HiSeq 2000 platform.We performed 2 to 3 biological replicates for all drug treatment and knockdown conditions.

ChIP-seq

ChIP was performed as previously described (Iwase et al., 2016). We dissociated E18 mouse forebrains and culture them for 14 DIV, infected with lentivirus containing sh-*Rai1* #1 or sh-Ctrl. On DIV17, we treated cultures with 2 μM TTX, 20 μM BIC, or water vehicle for 4 h, harvested the cells, fixed with 1% formaldehyde in HBSS for 30 min at room temperature, and prepared chromatin samples. We digested chromatin first with MNase for 20 min at 25°C. We then spiked, *Drosophila* chromatin, which contains fly-specific histone variant H2Av (Active Motif Cat. No. 53083). Samples were then further sheared by sonication using Qsonica Q800R3 at 70% amplitude 15 s pulse with 20 s interval for 30 min (total time: 70 min). The antibodies applied were the abovementioned anti-RAI1 polyclonal and anti-*Drosophila* H2Av antibodies (2.5 μg/sample). Antibody-antigen complex that formed at 4°C overnight were precipitated with Dynabeads Protein A/G mixture (1:1, Invitrogen 10001D, 10003D). We isolated the pulled down DNA and made sequencing libraries with NEBNext reagents (E7645S) and sequenced them on the Illumina HiSeq4000 platform to generate 50 bp single-end reads.

Patch-Clamp Electrophysiology

Neurons were transfected with 1.0 μg of either sh-Ctrlor sh-*Rai1* #1 or #2. For the rescue experiments, an RNAi-resistant RAI1-expression plasmid or its empty vector were co-transfected with the above shRNA expressing plasmids. Transfections were performed using CalPhos Transfection kit (ClonTech) or Lipofectamine 2000 (ThermoFisher Scientific) according to the manufacturer's protocols. All experiments were performed 48 h after transfection. To induce synaptic scaling, neurons were treated with either 1 μM TTX, 10 μM bicuculine or vehicle for 24hr prior to recording. mEPSCs were recorded from a holding potential of – 70 mV with an Axopatch 200B or Multiclamp 700B amplifier from neurons bathed in HEPES buffered saline (HBS) containing: 119 mM NaCl, 5 mM KCl, 2 mM CaCl2, 2 mM MgCl2, 30 mM Glucose, 10 mM HEPES (pH 7.4) plus 1 μM TTX and 10 μM bicuculline.

Multi-Electrode Array Electrophysiology

On DIV11, neurons were transfected with lentivirus encoding sh-Ctrl or sh-*Rai1* #1 or #2 by performing a half-media change. On DIV14, Local Field Potential (LFP) recordings were acquired at 20 kHz using a MEA2100-System (Multichannel Systems, Reutlingen, Germany). MEA chips were secured to the headstage of the amplifier and maintained in a controlled environment (37°C, 5% CO2) for the duration of the recording. Prior to recording, MEAs were undisturbed for eight min to allow for acclimation after handling.

Immunofluorescence

Surface GluA1 staining was conducted as previously described with slight modification (Henry et al., 2012). On DIV12, rat cultured hippocampal cells were infected either with lentivirus carrying sh-Ctrl or sh-*Rai1* as described above. After 72 h of incubation, cultured cells were live-labeled with rabbit anti-GluA1 antibody (10 μg/ml, EMD Millipore, ABN241) for 20 min at 37°C, fixed with 2% paraformaldehyde, and further labeled with mouse anti-PSD-95 (EMD Millipore, MAB1596, 1:1000). Goat anti-mouse Alexa 488 and Goat anti-rabbit Alexa 555 secondary antibodies (Abcam, 1:500) were applied for 60 min at room temperature to visualize PSD-95 and GluA1 staining. Images of PSD-95 and GluA1 were acquired blinded tocondition using an inverted Olympus FV1000 laser-scanning confocal microscope using a Plan-Apochromat 63 X /1.4 oil objective.

For RAI1 and cell-type marker staining, two biological replicates of forebrain neuron cultures were obtained from E17.5 mouse embryos. On DIV19, they were fixed with 4% paraformaldehyde in 16% sucrose/PBS, permeabilized with 0.25% Triton-X in 1X PBS, blocked for 30 min with 10% bovine albumin serum (Sigma A2153), and overnight incubation of antibodies in 3% BSA at 4°C.Primary

antibodies used in the study are following. anti-NeuN (EMD Millipore, MAB377, 1:1000), anti-GFAP (NeuroMab N206A/8, 1:1000), anti-MAP2 (EMD Millipore, AB5543, 1:1000), anti-OLIG2 (EMD Millipore, AB9610, 1:1000), anti-CD11b (Abcam, ab133357, 1:500), anti-GAD67 (Santa Cruz, sc-5602, 1:1000). Secondary antibodies (Invitrogen Alexa Fluor 488, 555, or 647) were applied for 45 min at room temperature. Fluorescence images were acquired blinded to condition using an Olympus BX61 fluorescence microscope (60X oil-immersion lens) and CellSense software.

Western Blot

To validate *Rai1*-KD in mouse forebrain neuron culture, *Rai1*-KD and control cultures were harvested at 3 days after lentiviral transduction and subjected to western blot analysis as described previously (Iwase et al., 2016). RAI1 antibodies were generated by immunizing rabbits with a synthesized RAI1 peptide (aa 28 to 42, ENYRQPGQAGLSCDR, Thermo Fisher Scientific), followed by affinity purification using the peptide as the affinity ligand (Thermo Fisher Scientific). Anti-PCNA antibody (Santa Cruz sc-56, 1:1000) was used for a loading control. For analysis of RAI1 level during activity shifts, the cortices from E18.5 rat pups were dissected, dissociated, and plated at 700,000 cells/well in a PDL-coated 6-well dish. Neurons were grown in Neurobasal/B27 medium for 14 DIV. Vehicle (1% water), TTX (1 μM) or BIC (20 μM) were added to the culture and cells were harvested with a 1:1 mixture of 2X Laemmeli buffer (BioRad, 1610737, 1:20 beta-mercaptoethanol) and radioimmunoprecipitation assay (RIPA) buffer supplemented with 50 mM BGP and 1 mM Na3VO4. Protein samples were boiled for 10 min at 100°C. 10-15 μg of each sample was loaded per lane, separated by 7.5% SDS-PAGE, and transferred onto PVDF membrane (Millipore IPVH00010). Membranes were then blocked with 5% skim milk or 3% blotting-grade blocker (BioRad 1706404) for 1 hr, probed overnight with the following primary antibodies diluted in 3% BSA (Fisher Scientific BP1600): RAI1 (1:1000), beta-actin (Sigma A5441, 1:20,000). Horseradish peroxide (HRP)-conjugated secondary IgG antibodies (EMD Millipore AP132P or AQ160P) were also diluted in 3% BSA, and the HRP signal was developed with various chemiluminescent substrates from Thermo Fisher Scientific (34080 or 34095) and Li-COR Biosciences (926-95000).

QUANTIFICATION AND STATISTICAL ANALYSIS

Bru-seq Activity-Induction

After confirming the quality of sequencing data by FastQC, reads were mapped to mm9 reference genome using Bowtie2 (Langmead and Salzberg, 2012) and annotated with Tophat2 (Kim et al., 2013). Adaptors were trimmed using BBDUK (https://jgi.doe.gov/data-and-tools/bb-tools/), when 2-30 bp on the left of the read matched the predicted adaptor (k = 30, mink = 2, minlength = 15, hdist = 1). Bru-seq signals were quantified by FeatureCounts (Liao et al., 2014). We excluded *Rn45s*, *Lars2*, *Rn4.5 s*, *Cdk8*, *Zc3h7a* and the mitochondrial chromosome to avoid counts of overamplified genes that may skew RPKM normalization. DE-genes were identified using DESeq2 (Love et al., 2014) using the same parameters for the Bru-seq data and three published mRNA-seq datasets of neuron culture and *Rai1*-KO mice (Huang et al., 2016; Schaukowitch et al., 2017; Yu et al., 2015b). We also used DESeq2 to calculate RPKM expression values across the entire genic regions, including introns. Correlation analyses used base R Spearman Rank correlation test coupled with t tests to avoid the effect of extreme outliers (Figures 2, 4 and S5). Fold change comparisons were tested using the non-parametric Wilcoxon rank-sum/Mann-Whitney U test (Figures 1 and 4) Gene ontology was examined using RNA-Enrich (Lee et al., 2016). Significance cutoff for reporting Sig-genes was an unadjusted p value < 0.05. We only presented GO terms that contain 5 to 250 genes.

ChIP-seq

Raw reads were demultiplexed and filtered according to the standard Illumina analysis pipeline. Reads from sequencing libraries were then mapped to the mouse (mm9) and fruit fly (dm6) genome assemblies using Bowtie1 (Langmead et al., 2009) allowing up to 2 mismatches. Only uniquely-mapped reads were used for analysis. We used MACS2 (version 2.1.0.20140616, FDR < 0.01) to identify RAI1 peaks using pooled input samples as a control (Zhang et al., 2008). For visualization in the UCSC browser, bigwig files were generated with coverage normalized using the number of mapped reads to the *Drosophila* genome (reads mapped per reference genome per million reads) (Egan et al., 2016; Orlando et al., 2014). ChIPseeker (Yu et al., 2015a) annotated RAI1 peaks to promoters, genic, or intergenic regions. We integrated following publically available epigenomic datasets: DNase I hypersensitive sites (DHS) of whole brain samples (Vierstra et al., 2014) (E14.5: GEO: GSM1014197, 8 week adult: GEO: GSM1014151), H3K4me1(ENCODE Project Consortium, 2012): whole brain (8 week: GEO: GSM769022, E14.5: GEO: GSM1000096), H3K4me3 (ENCODE Project Consortium, 2012): whole brain (8 week: GEO: GSM769026, E14.5: GEO: GSM1000095): H3K27ac (E14.5 whole brain (ENCODE Project Consortium, 2012)): GEO: GSM1000094, 8 week forebrain (Boxer et al., 2020): GEO: GSM3666438): and H3K27me (E14.5 H3K27me2 whole-brain (ENCODE Project Consortium, 2012): GEO: GSM1000143, 8 week H3K27me3 forebrain (Boxer et al., 2020), GEO: GSM3666437). Putative transcriptional enhancers were defined as DHS-positive RAI1 peaks (±500 bp) that overlap with H3K4me1 but not H3K4me3. Correlation analyses used base R Spearman Rank correlation test coupled with t tests to avoid the effect of extreme outliers (Figures 5 and S5). Enrichment analysis was tested using Chi-square test (Figures 5 and S5)

Patch-Clamp Electrophysiology

Miniature EPSCs were analyzed offline using MiniAnalysis. Statistical differences between experimental conditions were determined by unpaired Student's t tests (Figure 6) or one-way ANOVA followed by post hoc Fisher's LSD test (Figure 3).

Multi-Electrode Array Electrophysiology

Spontaneous activity was captured during 5 min epochs. Data were imported into MATLAB (MathWorks, Natick, MA) and analyzed using custom written scripts (https://github.com/Jcrd25/NeuroMEACode) The LFP signal was high pass filtered at 100 Hz using a Butterworth filter. Spikes were detected using amplitude thresholds set at five times the root mean square of the noise. Neuronal units were identified by spike sporting using principal component analysis of the detected spike and manually identifying clusters. A spike was defined by the signal 1 ms before the peak to 3 ms after the peak. The inter spike interval was defined as the time between two adjacent spikes. Mean firing frequency was calculated by dividing the total number of spikes detected for each neuronal unit by the recording duration. Statistical analyses were done in MATLAB and GraphPad Prism (GraphPad Software, San Diego, CA). Kruskal-Wallis test followed by post hoc Dunn's multiple comparisons test were performed on data from three biological replicates.

Immunofluorescence

For RAI1 and cell-type marker staining, immunoreactivity was quantified blinded to condition and semi-automatedly using ImageJ after confirming specific staining by visual inspection.

For synaptic GluA1 staining, synaptic GluA1 was anlayzed on maximal intensity z-projections. Synaptic GluA1 was defined as a particle that occupied >10% of the PSD-95 positive area, and the average integrated intensity of synapatic GluA1 was calculated using custom-written analyses on ImageJ and MATLAB. Statistical differences between experimental conditions were determined by unpaired Student's t tests.

Western blot

Protein band intensity was visualized and quantified in the linear range using LI-COR C-Digit and Image Studio software. Three biological replicates were used. Results were compared using one-way ANOVA with Dunnett's test.